The Surface Energy Balance of Antarctic Snow and Blue Ice

RICHARD BINTANJA AND MICHIEL R. VAN DEN BROEKE

Institute for Marine and Atmospheric Research Utrecht, Utrecht University, Utrecht, the Netherlands

ABSTRACT

Little is known about the surface energy balance of Antarctic blue-ice areas although there have been some studies of the surface energy balance of snow surfaces. Therefore, a detailed meteorological experiment was carried out in the vicinity of a blue-ice area in the Heimefrontfjella, Dronning Maud Land, Antarctica, during the austral summer of 1992/93. Since not all the surface fluxes could be measured directly, the use of a model was necessary. The main purpose of the model is to calculate the surface and subsurface temperatures from which the emitted longwave radiation and the turbulent fluxes can be calculated. The surface energy balance was evaluated at four locations: one on blue ice, and three on snow. Differences are due mainly to the fact that ice has a lower albedo (0.56) than snow (0.80). To compensate for the larger solar absorption of ice, upward fluxes of longwave radiation and turbulent fluxes are larger over ice. Moreover, the energy flux into the ice is larger than into snow due to the differences in the radiative and conductive properties. Surface temperatures, snow subsurface temperatures, and ice sublimation rates evaluated with the model compare well with the measurements, which yields confidence in the surface energy balance results. The latent heat flux is particularly important since the spatial variability of the sublimation rates largely influences the extent of a blue-ice area. This study helps to explain the heat exchange processes over Antarctic surfaces.

1. Introduction

Antarctica is generally known as the white continent since nearly 98% of its area is covered with snow. Only small parts are snow-free, such as dry valleys and blue-ice areas (BIAs, hereafter). The local surface mass balance of these specific areas is negative. Their surface area is too small to play an important role in the total surface mass balance regime of Antarctica. However, on a regional scale they can be quite important for the mass balance and therefore for the ice flow. BIAs seem to be relatively widespread, especially in mountainous regions (Schytt 1961; van Autenboer 1964; Budd 1967; Takahashi et al. 1988). On the leeward side of mountains, conditions seem to be favorable for the existence of BIAs. The main processes determining the mass balance of these areas are 1) low snow accumulation rates due to a small snow-drift divergence in the wind shadow of mountain ridges and 2) high ablation rates, mainly through sublimation. These high sublimation rates are closely connected with the local surface energy balance (SEB, hereafter) of BIAs. The local SEB is dependent on a number of variables, such as 1) the local wind field, which determines the latent and sensible heat fluxes, 2) air temperature and humidity, which also determine the heat and moisture fluxes between

Corresponding author address: Dr. Richard Bintanja, Institute for Marine and Atmospheric Research Utrecht, P.O. Box 80.005, 3508 TA Utrecht, the Netherlands.
E-mail: nbintanj@fys.ruu.nl

the surface and the atmosphere, 3) cloudiness, which determines the radiation balance, and 4) surface albedo, which also influences the radiation balance. The extent of a BIA, which is determined by the horizontal mass balance variations, is therefore dependent on many variables. Orheim and Lucchitta (1990) demonstrate the possibility to determine temporal changes in the extent of a BIA by satellite. The results of this study can be regarded as a first step to interpret such changes in terms of (local) climate change.

The main purpose of this paper is to present a detailed study of the SEB of blue ice and of snow during summer. The focus will be on the spatial variability of the SEB in the vicinity of a BIA. All components of the SEB, such as radiation balance, turbulent fluxes, and subsurface energy fluxes, are quantified. Measurements as well as modeling results will be presented. Further, the influence of the specific characteristics of a BIA on the sublimation rate (and hence on the mass balance) will be discussed.

2. Location

The Swedish research station Svea (74°35'S, 11°13'W, 1250 m MSL) was used as base camp. The authors stayed there from 23 December 1992 to 12 February 1993 as part of SWEDARP (Swedish Antarctic Research Programme). The measurements were made in the vicinity of a 2 km × 5 km BIA in a U-shaped valley called Scharffenbergbotnen in the central part of the Heimefront Range. It is located approxi-

mately 290 km from the coast in Eastern Queen Maud Land (Fig. 1). Smaller BIAs are located in the areas surrounding the valley. According to Worsfold (1967), the BIA in the valley of Scharffenbergbotnen is the largest in the central Heimefront Range.

A steady inflow of ice into the valley, mainly through the broad northwestern entrance and the smaller western passage near Svea, counteracts the mass loss through sublimation. This results in a southeast-directed ice flow inside the valley, whereas the large-scale flow is directed northwestward. The ice thickness is approximately 1000 m at the northwest entrance, as determined by radio-echo soundings (Herzfeld and Holmlund 1990). The annual ablation is largest in the eastern part of the valley, where it amounts to 0.15-m water equivalent (w.e.). Most of the ablation takes place in summer, although, according to Jonsson (1992), the wintertime ablation cannot be neglected

entirely. The mean annual accumulation rate on the adjacent plateau Ritscherflya is 0.16 m w.e. and increases to approximately 0.40 m w.e. on the coastal ice shelves (Jonsson 1992; Lunde 1961).

The large-scale slope direction is 140°, which induces a large-scale wind with dominant wind direction of 80° (Jonsson 1992). Measurements from January to February 1988 in Scharffenbergbotnen show a mean wind speed of 4.4 m s^{-1} with strong gusts. Temperatures were −4.7°C inside the valley, 2.4° warmer than outside the valley (to·the northwest). The relative humidity inside the valley was 57% and approximately 65% outside. This indicates that the mean specific humidity inside the valley is somewhat higher than outside, probably due to the relative high sublimation over the blue ice. These differences indicate that in the vicinity of a BIA, large differences in meteorological variables can occur over only a few kilometers. Thus,
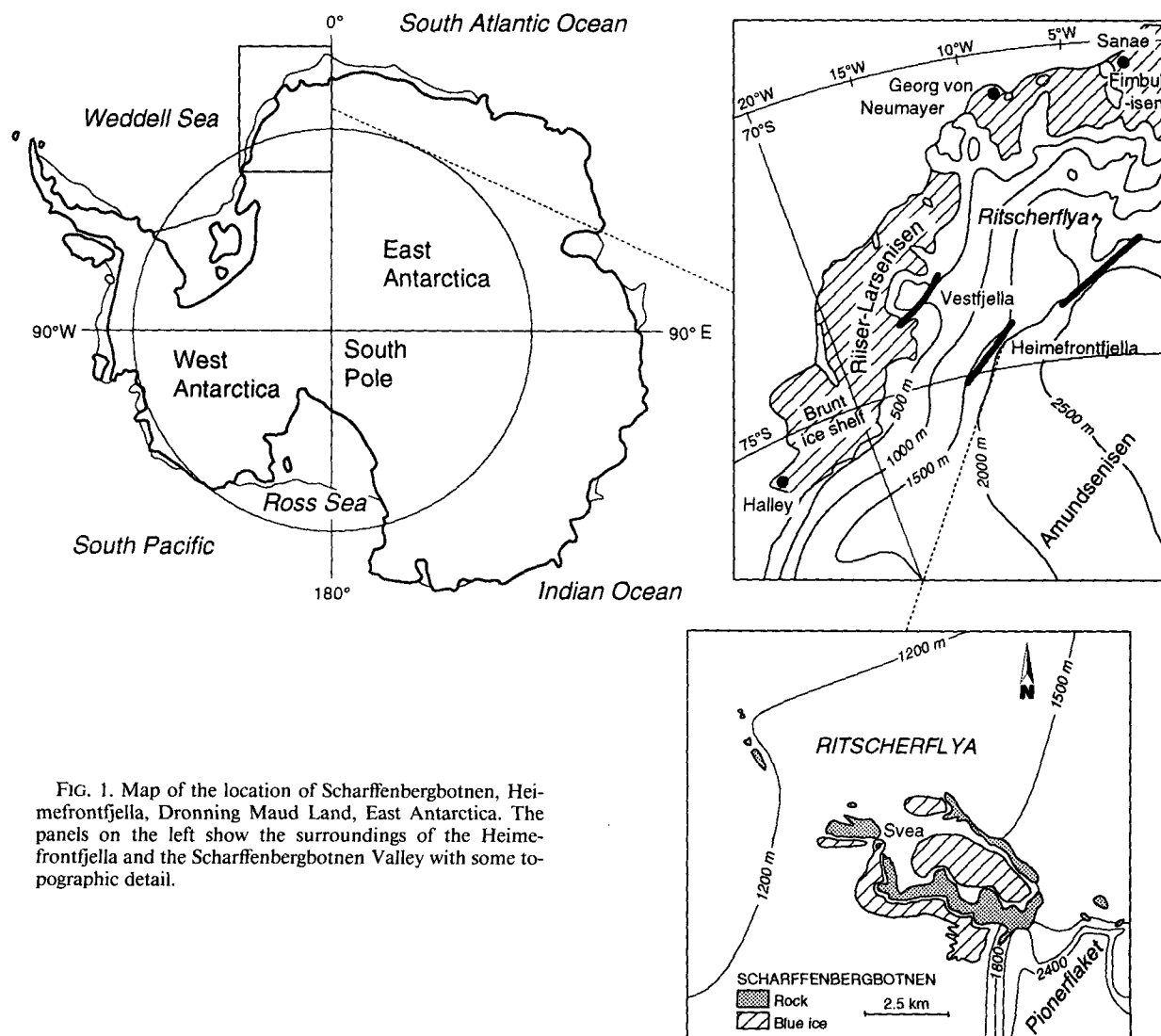

FIG. 1. Map of the location of Scharffenbergbotnen, Heimefrontfjella, Dronning Maud Land, East Antarctica. The panels on the left show the surroundings of the Heimefrontfjella and the Scharffenbergbotnen Valley with some topographic detail.

horizontal homogeneity will in general not be found in the vicinity of BIAs, which hampers the interpretation of the SEB results.

The Scharffenbergbotnen BIA seems to resemble the majority of other BIAs listed in the literature since it is located on the leeward side of a mountain ridge and has a pronounced local climate as compared to nearby snow-covered areas. Therefore, it is expected that qualitative conclusions drawn from measurements at this location can be applied more generally to other BIAs.

3. Instrumentation and data acquisition

Spatial variations in surface type (snow, rock, blue ice) occur over only a few kilometers in the vicinity of a BIA. Therefore, spatial variations in the meteorological conditions and in the SEB can be captured only by a dense net of measuring sites. Meteorological masts were placed at seven sites in and around the Scharffenbergbotnen Valley (Fig. 2). Sites 2 and 3 were located inside the valley on blue ice and on snow, respectively. Sites 4 and 5 were located on the lower plateau Ritscherflya, and site 1 on the higher plateau Pionerflaket. Finally, two additional measuring sites (6 and 7) were located on small BIAs on the western

side of the valley. In this way, the local valley regime (sites 2 and 3), the relatively undisturbed plateau regimes (sites 4, 5, and 1), and the regime of the downwind side of the valley (sites 6 and 7) could be studied. Unfortunately, a heavily crevassed area prevented us from taking measurements on the upwind (eastern) side of the valley.

The instrumentation was essentially the same as used in earlier expeditions to the Alps, King George Island (Antarctica), and Greenland (Oerlemans and Vugts 1993). The experimental setup and data acquisition routine are described in detail in Bintanja et al. (1993) and will only be summarized here. The measurements covered approximately a six-week period from 31 December 1992 to 10 February 1993. At all sites, masts were placed containing wind speed (2- and 6-m height), wind direction (6 m), and temperature (2 and 6 m) sensors. At sites 2, 3, and 7, relative humidity was measured at 2 and 6 m. Masts at sites 2 and 3 were equipped with additional temperature and humidity sensors at 0.5 m. The temperature and humidity sensors were ventilated and shielded from radiation. At sites 1, 2, 3, 5, and 7, shortwave incident and reflected radiation (1.5 m) were measured. Total radiation (1.5 m) was measured at sites 2 and 3. At site 3, snow temperatures
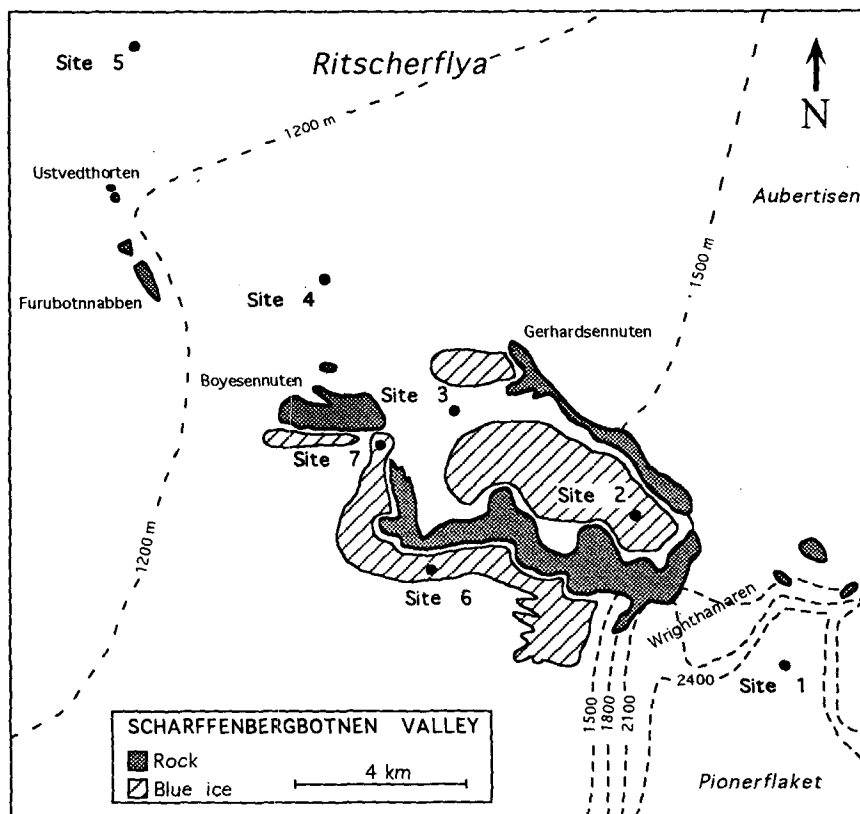

FIG. 2. Location of the measuring sites in and around the Scharffenbergbotnen Valley.
Site 7 is situated near base camp Svea.

were measured at five levels (i.e., -5, -10, -20, -40, and -80 cm). The equipment at site 2 is shown in Fig. 3. The sampling frequency of all sensors was 2 min. Data were transmitted to the base camp by radio about every hour where they were stored and analyzed. In this paper, only data from sites 2, 3, 4, and 5, which were located on a straight line parallel to the main axis of the valley (southeast–northwest), were used. Table 1 shows some characteristics of these measuring sites. At site 2 and especially site 5, electronic problems caused some loss of data.

The precision of the sensors was estimated in various test campaigns (before and during the expedition). The estimated precision for air temperature was $\pm0.2°C$, for relative humidity $\pm2\%$, for wind speed ±0.2 m s^{-1}, for wind direction $\pm3°$, for shortwave and total radiation 2% (daily average), and for snow temperature $\pm0.05°C$. Analysis of data obtained during earlier field campaigns revealed that the total radiation sensors suffered from a systematic offset of -10 to -20 W m^{-2}. This underestimation of the total radiation was corrected for in the present study, as will be discussed below.

A cable balloon system was used at Svea (near site 7) to obtain vertical profiles of temperature, humidity, wind speed, wind direction, and pressure in the lowest 1200 m of the atmosphere. The soundings were performed every 6 h provided weather conditions were

TABLE 1. Characteristics of the measuring locations studied in this paper.

Site	Surface type	Elevation (m MSL)	Distance from site 2 (km)	Performance (%)
2	blue ice	1170	0	90
3	snow	1260	5	100
4	snow	1200	9	100
5	snow	1150	16.5	63

good. They were increased to every 3 h on nine selected days.

Cloud observations (type and amount) were performed every 3 h at the base camp. These observations are assumed to be valid for the entire valley (sites 2, 3, and 7).

At sites 2 and 3, surface temperature measurements were made during some selected periods. A downward-facing infrared radiation sensor and a resistance thermometer placed at the surface were used. As these sensors were not ventilated, the reliability of the measurements varied considerably with time. It was only during periods with high wind speeds when the errors due to heating of the instruments by direct radiation were small. Measured surface temperatures obtained on those days are used for comparison with model results.
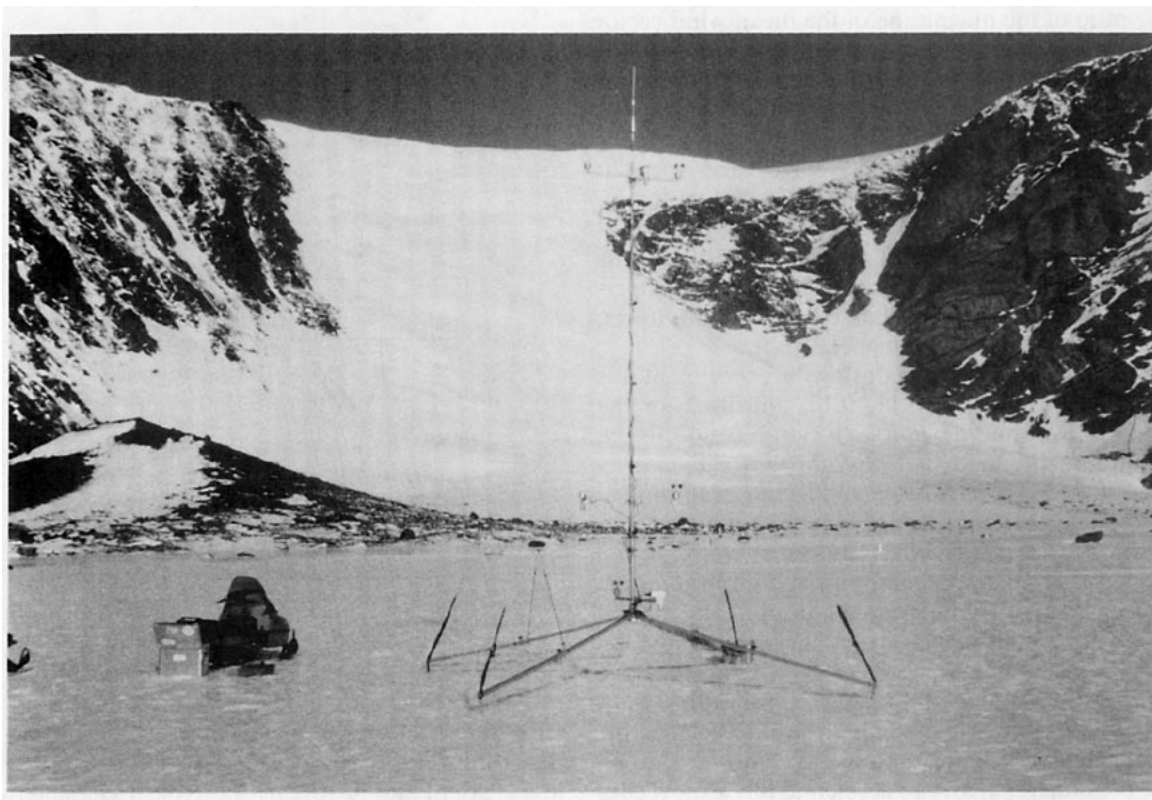

FIG. 3. Photo of the measuring equipment at site 2 at blue ice.

4. Meteorological conditions

The weather during the six-week measuring period consisted of a succession of calm, sunny periods and windy overcast conditions. Figure 4 shows some meteorological quantities. The windy periods are connected to depression activity near the coast, which intensified the large-scale easterly katabatic wind. During these periods, humid air was advected inland and some precipitation occurred. The calm periods are associated with low cloud amounts and westerly winds inside the valley. Table 2 lists mean and extreme data for the measuring period. The temperature decreases 3.1°C going out of the valley; this decrease cannot be attributed to differences in elevation. The temperature variations are most pronounced at night (Fig. 5c), which can be explained qualitatively by variations in the local SEB, as will be discussed later on. Also, the heating of rocks inside the valley contributes to the warm valley climate. The mean summertime relative humidity is rather low compared to the value of 80%–90% at nearby coastal stations Halley and Sanae (Schwerdtfeger 1970), which can be attributed to the different origin of the prevailing air masses (moist ocean air versus dry inland air). The difference between the mean relative humidity at sites 2 and 3 is negligible.

The mean wind speed decreases from site 5 to site 3 but increases again toward site 2. Outside the valley (sites 4 and 5), the wind blows almost permanently from the east with high directional constancy (defined as the ratio of the magnitude of the mean wind vector to the mean wind speed) (e.g., Kodama et al. 1989). Inside the valley, the directional constancy drops below 0.7, a rather low value for Antarctic surface winds. The maximum wind speed is highest at site 2 due to strong gusts, which means that the average wind speed is higher than at site 3. To give an indication of the interannual variability at site 2, these values can be compared with mean quantities for January–February 1988 (Jonsson 1992): in the summer of 1992/93, temperatures were 3.5°C lower, relative humidity 5% lower, and wind speed 0.5 m s^{-1} higher.

The mean cloud amount during the experiment was 0.35, which consists of 0.11, 0.12, and 0.12 for the amount of low, middle, and high clouds, respectively. The amount of clouds is low compared with nearby coastal stations [0.7 at Halley and Sanae, according to Schwerdtfeger (1970)], which can be attributed to diminishing cyclonic activity associated with frontal clouds (e.g., stratus, stratocumulus and nimbostratus). Needless to say, the predominant amount and type of clouds determines to a large extent the surface radiation budget.

In the Antarctic coastal regions, a prevailing westward airflow occurs that results from the balance between inversion, friction, and Coriolis forces. A cross-shore pressure gradient can accelerate this airflow considerably. Figures 5a,b show some characteristics of
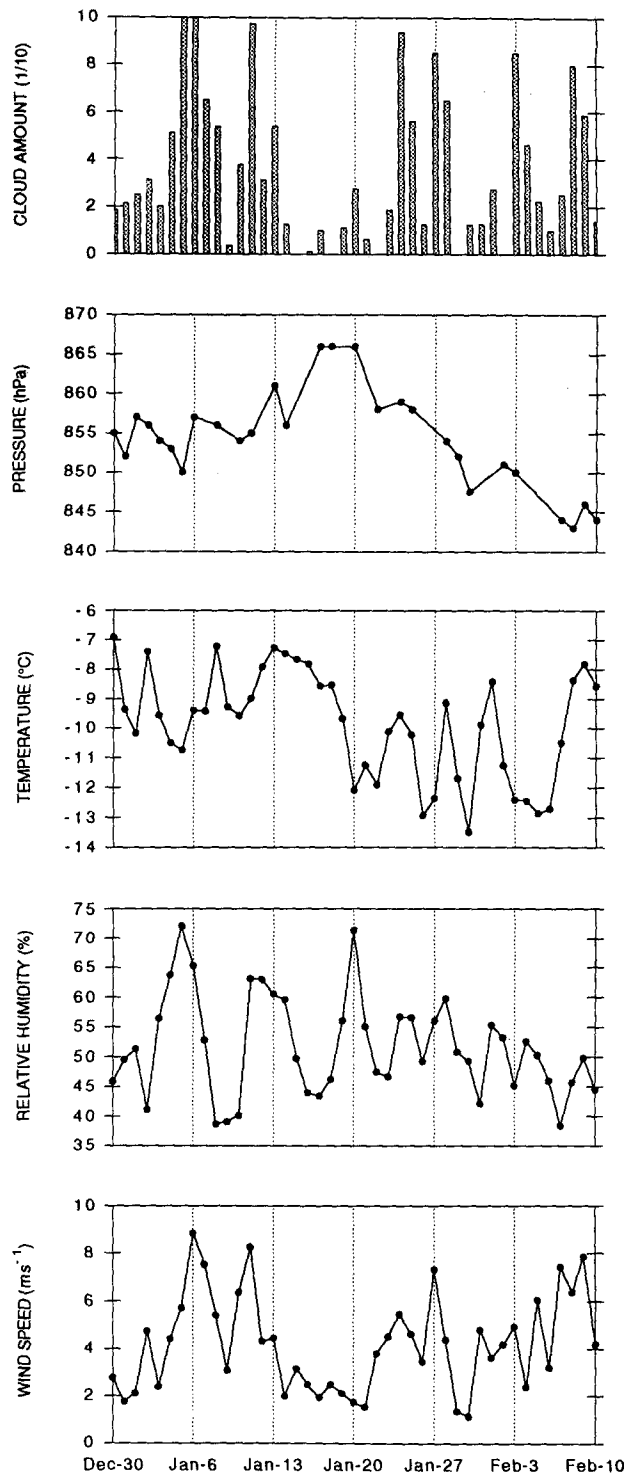

FIG. 4. Daily mean values of total cloud amount, pressure, temperature (2 m), relative humidity (2 m), and wind speed (6 m) at site 3.

the wind field for the various sites. Site 5, and to a lesser extent site 4, reveals the typical characteristics of the near-coastal surface airflow, as explained in detail

TABLE 2. Mean and extreme meteorological data for the period 28 December 1992–10 February 1993 evaluated from hourly mean values.

| Site | Temperature (°C) 2 m | | | Relative humidity (%) 2 m | | | Wind speed (m s^{-1}) 6 m | | Directional constancy 6 m |
	Min	Mean	Max	Min	Mean	Max	Mean	Max	
2	−17.1	−8.3	−1.9	24.3	51.5	81.4	4.9	15.9	0.65
3	−17.8	−9.8	−3.3	26.9	51.6	88.0	4.2	11.5	0.64
4	−20.1	−10.8	−2.0				5.2	13.7	0.84
5	−21.6	−11.4	−2.0				5.8	14.3	0.91

by Kodama et al. (1989) for Adelie Land, Antarctica. In the early morning the wind blows from the east with a maximum wind speed and a high directional constancy (0.95). In the afternoon the wind veers to the northeast, and its force and directional constancy decrease. This is due to extensive surface heating that causes unstable conditions and vigorous mixing; this in turn reduces the katabatic downslope force and turns the wind more in the direction of the geostrophic wind. The wind field at site 5, and to a lesser extent at site 4, can be considered as relatively undisturbed. At sites 2 and 3 inside the valley, the wind field is significantly different: the wind speed is at its maximum in daytime and at its minimum at night and the directional constancy is much lower. A high pressure system over the Weddell Sea causes weakening of the predominant easterly winds outside the valley and even causes occasional predominantly westerly winds inside the valley. This is best illustrated in Fig. 6, from which it can be inferred that noneasterly winds are more common inside the valley than outside. It can be concluded that the presence of the valley induces a very local wind regime, which further contributes to the spatial variability of the SEB.

5. Model description

a. General

The SEB over Antarctic snow surfaces has been widely studied (e.g., Schlatter 1972; Weller 1980; Carroll 1982; Ohata et al. 1985; Wendler et al. 1988). Also, the interaction between the SEB and the continental-scale katabatic wind has received much attention (e.g., Parish and Waight 1987; Kodama et al. 1989). The SEB of BIAs seems to be relatively unknown. There are some related studies but they focus mainly on the sublimation rate (Budd 1967; Fujii and Kusunoki 1982).

The surface energy balance equation can generally be written as (fluxes toward the surface positive)

$$S + L + H + LE + G = 0, \qquad (1)$$

where S is the net shortwave radiative flux [$S = (1 - \alpha_s)S_g$, with α_s the surface albedo and S_g the global radiation at the surface], L the net longwave radiative

flux, H and LE the turbulent sensible and latent heat fluxes, and G the total upward energy flux inside the snow/ice. The latter consists of a surface conductive heat flux G_c and a penetrating part of the shortwave radiation G_s. Melting was not observed at any of the four sites and is therefore not dealt with.

Obviously, all components of (1) should be known for a complete assessment of the SEB. Since not all SEB terms were measured directly, a simple model was applied (Knap 1992) to evaluate the remaining terms. A schematic representation of the model is given in Fig. 7. Essentially, the model evaluates the radiative and conductive fluxes and temperatures inside the snow/ice and the emitted longwave radiative and turbulent fluxes. At each site, hourly varying values of net shortwave radiation, incoming longwave radiation, wind speed, air temperature, and humidity are used as input to evaluate the nonmeasured SEB terms for the entire measuring period. All components of the model will be described below in more detail.

b. Subsurface heat and radiation transfer

In the absence of melting, refreezing of meltwater, and deformation, one can calculate the vertical temperature distribution in the interior of the snow/ice with the thermodynamic energy equation, which includes molecular diffusion as well as convective and radiative processes in the snow/ice:

$$\rho c_p \frac{\partial T}{\partial t} = -\frac{\partial G_c}{\partial z} + \frac{\partial S_i(z)}{\partial z}. \qquad (2)$$

Here, z is the coordinate normal to the surface (positive upward), ρ is the density of snow/ice, c_p is the specific heat capacity of ice at constant pressure (2×10^3 J kg^{-1} K^{-1}), T is the snow–ice temperature, $G_c = -K_s \partial T/\partial z$ is the conductive heat flux, K_s is the conductivity of snow/ice, and $S_i(z)$ is the penetrated shortwave radiation at depth $-z$. Generally, the value of K_s is a function of density. For ice with a measured density of 850 kg m^{-3}, a value of K_s of 1.73 W m^{-1} K^{-1} is obtained (Paterson 1981). For snow, the value of K_s is determined from snow temperature measurements at site 3 (see appendix A). For the measured value of the snow density of 400 kg m^{-3}, K_s is found to be 0.25
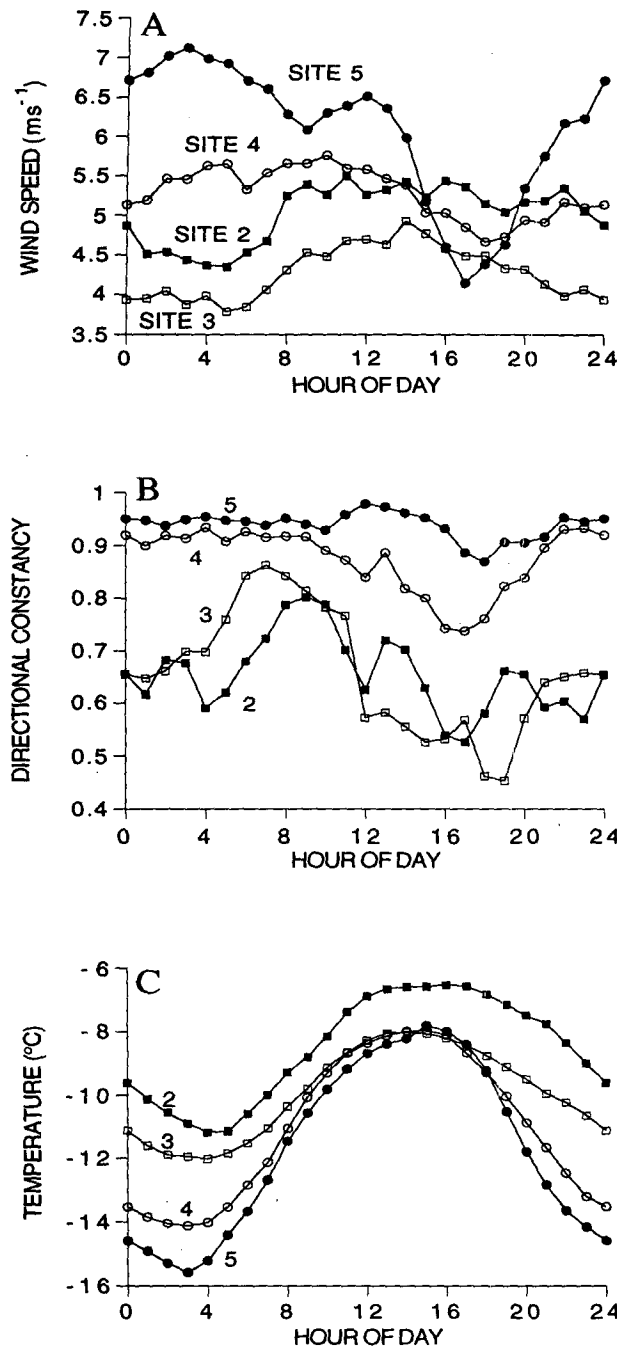
FIG. 5. Mean diurnal cycle of (a) wind speed (6 m), (b) directional constancy (6 m), and (c) temperature (2 m) at sites 2, 3, 4, and 5 for the period 1 January–10 February 1993.

FIG. 6. Relative occurrence (percentage of time) of wind direction in 10° intervals for (a) site 3 and (b) site 5 during the measuring period.

$\pm$ 0.03 W m^{-1} K^{-1}, which is somewhat smaller than values reported in the literature. This value is used for the evaluation of the conductive heat flux at sites 3, 4, and 5.

c. *Shortwave radiation*

The spectrally integrated incoming and reflected shortwave fluxes were measured at sites 2, 3, and 5 at

1.5-m height. However, the radiative fluxes inside the snow/ice were not measured. For a correct treatment of this process, one has to take into account the spectral

FIG. 7. Schematic representation of the surface energy balance model. Measured fluxes and meteorological quantities (T_a, RH, and U indicate air temperature, relative humidity, and wind speed, respectively) are outlined. The other variables and fluxes are evaluated with use of the model.

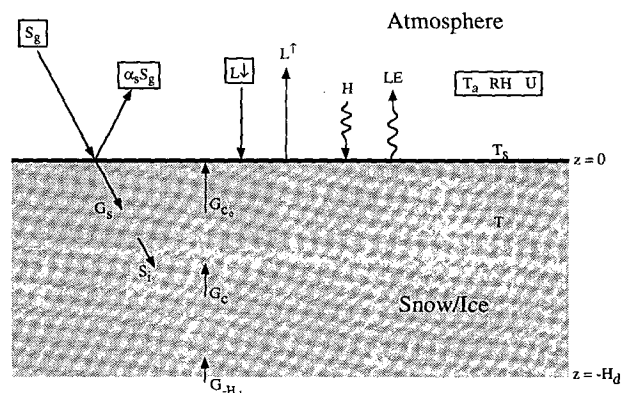dependence of the optical properties of ice and snow. According to Wiscombe and Warren (1980), the absorption is highest in the near-infrared and almost zero in the visible part of the spectrum. Brandt and Warren (1993) show that a significant part of the absorption (>50%) of near-infrared radiation occurs in the top few millimeters of the snow/ice. Thus, the extinction coefficient decreases significantly with depth, especially close to the surface. To account for this, the extinction of solar energy in the snow–ice layers is parameterized in the following way: in the top model layer, a fraction ζ is absorbed, and below that, an exponentially decreasing flux with constant extinction coefficient β is assumed. Thus, the shortwave flux at depth $-z$ can be expressed as (downward positive)

$$S_i(z) = S(1 - \zeta)e^{\beta z}. \qquad (3)$$

Thus, the downward-directed surface radiative flux G_s is equal to $(1 - \zeta)S$. With this simple approximation, the basic properties of subsurface radiational heating, as obtained from sophisticated two-stream radiative transfer models (e.g., Brandt and Warren 1993), can effectively be simulated. This method was used before by Greuell and Oerlemans (1989) and Knap (1992). Values of ζ and β are listed in Table 3.

Wiscombe and Warren (1980) show that the (spectral) albedo (and thus the extinction coefficient) is generally dependent on snow-grain radius, solar zenith angle, and the presence of clouds. Although it is acknowledged that these factors may be important, they are neglected in the parameterization of the extinction coefficient.

d. Longwave radiation

The longwave radiation components have been derived from the total and shortwave radiation measurements at sites 2 and 3. Unfortunately, the usage of the total radiation sensors leads to an underestimation of the incoming longwave radiation $L^\downarrow$, as referred to in section 3. Comparison of measured clear-sky values of $L^\downarrow$ with those from the empirical relationship of Kimball et al. (1982) shows that the order of magnitude of the offset is -10 to -20 W m^{-2}, while the diurnal and day-to-day variability seems to be reasonably good. Therefore, a constant correction will be added to the incoming longwave radiation that will be used as a tuning parameter, as will be described in section 5f.

The infrared radiation emitted by the surface $L^\uparrow$ is calculated from the surface temperature T_s with

$$L^\uparrow = \epsilon\sigma T_s^4, \qquad (4)$$

where σ is Boltzmann's constant ($=5.667 \times 10^{-8}$ W m^{-2} K^{-4}). It is assumed that the surface emissivity ϵ for snow and ice equals unity.

e. Turbulent fluxes

The transport of heat and moisture in the lowest layers of the atmosphere (surface layer) is dominated by turbulent motions. The turbulent sensible and latent heat fluxes can be calculated with the Monin–Obukhov similarity theory. According to this theory, the mean gradients of wind $\mathbf{v} = (u, v)$, potential temperature θ, and specific humidity q in the surface layer are related to the corresponding fluxes as

$$\frac{\kappa z}{u_*}\frac{\partial |\mathbf{v}|}{\partial z} = \phi_m(\xi) \qquad (5a)$$

$$\frac{\kappa z}{\theta_*}\frac{\partial \theta}{\partial z} = \phi_h(\xi) \qquad (5b)$$

$$\frac{\kappa z}{q_*}\frac{\partial q}{\partial z} = \phi_h(\xi), \qquad (5c)$$

TABLE 3. Characteristics of the assumptions and measurements used for the SEB calculation. An asterisk (*) indicates that the variable is measured locally.

	Site 2	Site 3	Site 4	Site 5
Number of days	37	41	41	26
Snow–ice density ρ (kg m^{-3})	850	400	400	400
z_{0m}, z_{0h}, z_{0q} (mm)	0.007	0.084	0.550	0.750
ζ	0.8	0.9	0.9	0.9
β (m^{-1})	2.5	17.1	17.1	17.1
K_s (W m^{-1} K^{-1})	1.73	0.25	0.25	0.25
L_{corr} (W m^{-2})	10	20	20	20
G_{-H_d} (W m^{-2})	-2	-2	-2	-2
Initial snow–ice temperature	$-8°$C	*	from site 3	from site 3
Integration depth H_d (m)	3.2	0.8	0.8	0.8
RH values	*	*	RH site 3 + 3.5%	RH site 3 + 7.5%
$L\downarrow$ values	*	*	from site 3	from site 3
S values	*	*	from site 3	*
Height WSP (m)	2.12	2.12	2.09	2.09
Height T_a (m)	0.82	0.70	1.88	1.88
Height RH (m)	0.82	0.70	1.88	1.88

where κ is the von Kármán constant ($=0.4$) and z the height above the surface. The characteristic scales of velocity, potential temperature, and specific humidity are given by u_*, θ_*, and q_*, respectively, and are related to the variances u', v', w', θ', and q' as

$$u_*^2 = (\overline{u'w'}^2 + \overline{v'w'}^2)^{1/2},$$

$$u_*\theta_* = -\overline{w'\theta'}, \quad u_*q_* = -\overline{w'q'}. \quad (6)$$

In (5a)-(5c), ξ is the nondimensional length scale z/L_{mo}, in which L_{mo} is the Obukhov length scale defined as

$$L_{mo} = \frac{u_*^2}{\kappa(g/T_0)(\theta_* + 0.62T_0q_*)}, \quad (7)$$

where g is the acceleration of gravity and T_0 a reference temperature. The nondimensional stability functions ϕ_m and ϕ_h in (5a)-(5c) for momentum m and heat and moisture h are taken from the literature. For unstable conditions ($\xi < 0$), expressions given by Dyer (1974) and Högström (1988) are used:

$$\phi_m(\xi) = (1 - \gamma_m\xi)^{-1/4}$$

$$\phi_h(\xi) = (1 - \gamma_h\xi)^{-1/2}, \quad (8)$$

with $\gamma_m = 20$ and $\gamma_h = 15$. The stability corrections under stable conditions ($\xi > 0$) are far less certain, especially under very stable conditions. Here, the expressions given in Duynkerke (1991) are used, which are very similar to those proposed by Högström (1988) for moderately stable cases ($\xi < 1$):

$$\phi_m(\xi) = 1 + \chi_m\xi(1 + \chi_m\xi/a)^{a-1}$$

$$\phi_h(\xi) = 1 + \chi_h\xi(1 + \chi_h\xi/a)^{a-1}, \quad (9)$$

with $\chi_m = 5$, $\chi_h = 7.5$, and $a = 0.8$. It should be stressed that the values of χ_m and χ_h are far from certain. King (1990) shows that for the stable boundary layer overlying the ice shelf near Halley in the polar winter, the surface-layer similarity functions (9) cannot generally be applied except possibly for the lowest meters. In contrast to the midlatitudes, where expressions like (9) are derived, the background stability in the Antarctic winter is very large, which reduces the boundary layer depth ($\ll 100$ m). Therefore, the turbulent length scales are severely reduced and the scaling assumptions implicitly included in (9) lose their validity. In summer, however, the very large background stability is replaced by a moderately stable boundary layer. Daytime mixing reduces its stability, which permits larger turbulent length scales throughout the nocturnal stable boundary layer (Sorbjan et al. 1986). Thus, it is expected that scaling functions like (9) are applicable to higher levels during the Antarctic summer. Figure 8 shows examples of the average potential temperature profile for the period 14–19 January. In accordance with Sorbjan et al. (1986) and Kodama et al. (1989), typical depths of
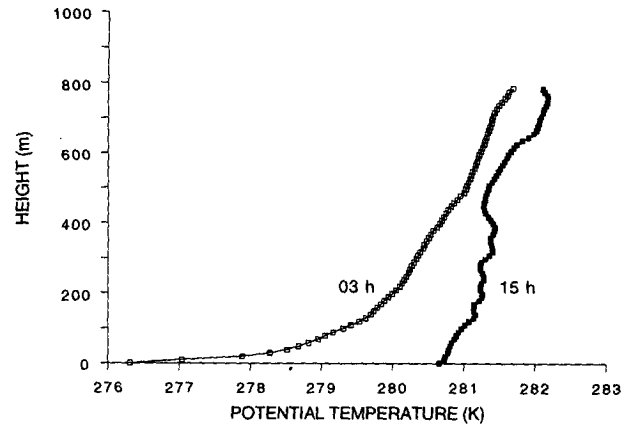

FIG. 8. Mean vertical profile of potential temperature at 3 and 15 h for the period 14–19 January. This period was characterized by fair weather, that is, light winds and low cloud amounts.

the nocturnal stable boundary layer and the near-neutral mixed layer in daytime are 200–500 m. The overlying atmosphere is moderately stable with a potential temperature gradient of 2.6 K km^{-1}.

In the atmospheric surface layer, the fluxes, and therefore the characteristic scales u_*, θ_*, and q_*, are assumed to be constant with height. Then, the flux profile relations (5a)-(5c) can be integrated analytically between two heights. The fluxes of sensible heat $H = -\rho_a c_{pa} u_* \theta_*$ and latent heat $LE = -\rho_a L_s u_* q_*$ follow from measurements of wind speed, potential temperature, and specific humidity at two heights in the surface layer ($\rho_a = 1.15$ kg m^{-3} is the density of air at 1250 m MSL, $c_{pa} = 1004$ J kg^{-1} K^{-1}, the specific heat capacity of air at constant pressure, and $L_s = 2.842 \times 10^6$ J kg^{-1}, the latent heat for sublimation). Note, however, that wind speed, temperature, and humidity do not have to be measured at the same heights.

Although the Monin–Obukhov theory can be applied to derive fluxes from measurements at two heights in the atmosphere, this will sometimes lead to large errors in the fluxes. As an example, the dependence of the sensible heat flux on potential temperature and wind speed differences between 2 and 6 m is given in Fig. 9. It is clear that especially in the unstable surface layer the flux increases rapidly with increasing $\Delta\theta$. In fact, uncertainties in $\Delta\theta$ of the order of 0.3°C, which is normally the maximum accuracy one can expect, will lead to variations in the sensible heat flux of 100 W m^{-2} or more. Similar arguments can be given with respect to the latent heat flux. Since errors of such magnitude are clearly unacceptable, the turbulent fluxes are calculated by applying (5a)-(5c) between a level in the atmosphere and the surface. Temperature and humidity differences between this height and the surface will certainly be large enough to keep the errors in the turbulent fluxes relatively small. At the surface, the wind speed is zero and it is assumed that the surface air is saturated with respect to ice.
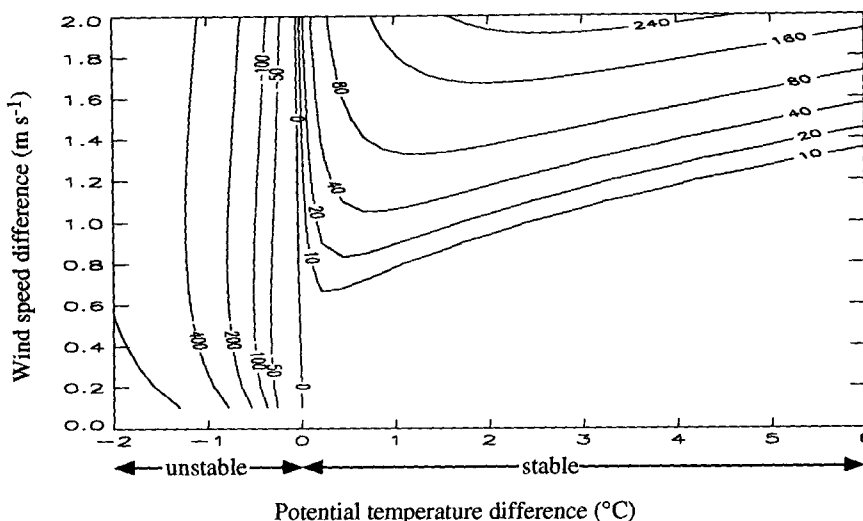
FIG. 9. Values for the sensible heat flux $H = -\rho c_{pa} u_* \theta_*$ (W m^{-2}) as a function of the wind speed and potential temperature difference between 6 and 2 m ($\Delta\theta$). A value of $T_0 = -10°C$ was used and Δq was taken as 0. Note that for unstable conditions ($\Delta\theta < 0$), H is almost only dependent on $\Delta\theta$.

The use of surface values means that it is essential to know the surface roughness lengths for momentum (z_{0m}), heat (z_{0h}), and moisture (z_{0q}). These are defined as the height where the downward extrapolated logarithmic profiles of wind speed, potential temperature, and specific humidity reach their surface values. This procedure is easy for wind speed since its surface value is equal to zero. Table 3 lists the aerodynamic roughness lengths at each site, derived from 2- and 6-m measurements under adiabatic conditions ($|z/L_{mo}|$ ≤ 0.03) and assuming a logarithmic wind profile. Going from site 2 to 5, there is an increase in roughness length of two orders of magnitude. The momentum roughness length of blue ice (site 2) is of the order of the diffusion roughness length $\nu/u_* \approx 10^{-5}$ m (ν is the molecular diffusion coefficient) (Brutsaert 1982), which indicates that the airflow over blue ice is in the aerodynamically smooth regime. A similar small value for the momentum roughness length (0.024 mm) was found on the BIA on the western side of the valley (site 6), which is an indication of the fact that the distances to upstream rock outcrops are probably large enough for the growth of a constant-flux layer deeper than 6 m, which is entirely determined by the stress at the ice surface (the value of z_{0m} at sites 2 and 6 can be regarded as characteristic for blue-ice surfaces). Blue ice probably has the smoothest (permanent) surface found in nature. Values of z_{0m} over snow surfaces at site 3, 4, and 5 are comparable with those found in the literature (e.g., Fujii and Kusunoki 1982; Kondo and Yamazawa 1986; Wendler et al. 1988; King 1990). The increase of z_{0m} toward site 5 can easily be explained by the increase in the geometrical roughness due to the presence of larger surface elements (sastrugis) outside the valley.

Generally, z_{0m} will depend on u_* over smooth surfaces (sites 2 and 3), as was found in experimental studies (Brutsaert 1982). Since mainly measurements with large wind speeds (hence large u_*) were used to determine z_{0m}, its value will be a low estimate at sites 2 and 3. On the other hand, Wendler (1989) concluded from wind profiles during drifting snow that z_{0m} increases with wind speed. In the present study, z_{0m} is assumed to be constant in time since any dependence of z_{0m} on u_* will be submerged in the large scatter that is inevitably present using wind speed profiles over relatively smooth surfaces. For the present purpose, this seems to be a reasonable approach given all the uncertainties.

The values of z_{0h} and z_{0q} are even more difficult to obtain. Very near the surface, the scalar transport is determined only by molecular diffusion, whereas over rough surfaces, momentum is transferred by means of pressure forces (form drag). According to Brutsaert (1982), theoretical and experimental studies show that over smooth surfaces the scalar roughness lengths are of the order of the momentum roughness length. However, over rough surfaces, z_{0h} and z_{0q} will be significantly smaller than z_{0m}. Since local values of z_{0h} and z_{0q} could not be derived from measurements, it is assumed that they equal z_{0m}, which is thus probably correct for smooth surfaces (sites 2 and 3). Over rough snow surfaces (sites 4 and 5), however, this may induce an overestimation of the turbulent fluxes.

f. Numerical procedure, assumptions, and tuning

At the upper boundary of the snow–ice pack, the exact formulation of (1) is valid, which is therefore applied to the uppermost model layer:

$$\zeta S + L + H + \text{LE} + G_{c_0} = 0, \qquad (10)$$

where G_{c_0} is the conductive heat flux just below the surface. The total surface energy flux into the snow/ice (G) consists of a conductive and a radiative part (positive upward):

$$G = G_{c_0} - G_s = -K_s \frac{\partial T}{\partial z}\bigg|_{z=0} - (1 - \zeta)S. \qquad (11)$$

The longwave radiative flux and the turbulent fluxes influence only the top few millimeters of the snow/ice and are therefore present only in (10) and not in (2). In the numerical procedure, where the surface is represented by the uppermost model layer, G is the flux between the two uppermost model layers. The conductive heat flux at the lower boundary (G_{-H_d}) is assumed to be constant in time and the radiative flux at $z = -H_d$ is negligible for values of H_d as depicted in Table 3.

At each site, the model is forced with local hourly mean values of the shortwave radiation fluxes and the incoming longwave radiative flux (Table 3) for the entire 41-day measuring period from 1 January to 10 February. For the evaluation of the turbulent fluxes, wind speed, temperature, and relative humidity measurements from one level are used. Equation (2) is solved numerically on an equidistant vertical grid (grid distance 5 mm) on which the space derivative is discretized with central differences. At site 3, the measured snow temperatures were used to initialize the model. Since the ice temperatures at site 2 were not measured, an isothermal initial temperature profile T_{init} of $-8°C$ was assumed. With an initial snow-ice temperature distribution, the associated longwave, turbulent, and conductive fluxes can be calculated. With all surface-air and subsurface energy fluxes known, the "new" (sub)surface temperature distribution is calculated from (2) and (10) for the next time step, after which the associated fluxes can again be calculated. Thus, with this methodology, subsequent values of all the SEB terms and the (sub)surface temperature distribution can be calculated for the entire period of measurements. The applied time step is 7.5 s, which means that all hourly input values are interpolated. When gaps in the input data occur, the SEB is not calculated. Note the great importance of the simulated surface temperature since it determines all surface fluxes except S, G_s, and $L^\downarrow$.

Humidity was not measured at sites 4 and 5. Fortunately, the measurements of summer 1988 described by Jonsson (1992) make it possible to crudely estimate the humidity at sites 4 and 5. In summer 1988, the average humidity outside the valley was approximately 7.5% higher than inside the valley. It is therefore assumed that with a correction of +7.5% the site 3 humidity values can be applied to site 5. Similarly, at site 4 a correction of +3.5% is assumed. It was realized,

however, that the humidity differences are not necessarily constant over the entire measuring period. The radiative fluxes from site 3 can be applied to sites 4 and 5 without causing large errors since 1) the spatial variation of cloud amount over the measuring region is observed to be very small, 2) shading of shortwave radiation by the mountains surrounding site 3 is negligible when daily means are considered, and 3) increased downward longwave radiation through heated rock surfaces is also negligible at site 3.

Another potential error can arise from erosion and/or deposition of snow that caused the ice at site 2 to be partially snow covered during some periods. Since accumulation is not included in the model, this will cause errors in the simulated surface temperatures and, accordingly, in the turbulent and longwave radiative fluxes. However, since accumulation was small and only temporary, the associated errors are expected to be small when average fluxes over the entire measuring period are considered.

The snow-ice density was measured at site 3 and site 2, respectively, and is assumed to be constant throughout the period. Accumulation and ablation caused variations in the sensor heights of only a few centimeters during the measuring period and can therefore be neglected.

The model is tuned with the correction to the incoming longwave radiation (L_{corr}) and the solar extinction coefficients ζ and β. At site 3, simulated snow temperatures should closely match the observed snow temperatures. At sites 2 and 3, observed surface temperatures were accurate enough on some days to use as reference for the model.

A complete list of the values used and the assumptions made to overcome the lack of measurements is presented in Table 3. Note that due to the lack of measurements the period of calculations at sites 2 and 5 was shorter than 41 days. Although all assumptions will introduce errors into the calculated SEB, especially at sites 4 and 5, it is not expected that results will deviate significantly from the true SEB. The sensitivity of the individual terms to the assumptions made and to measuring uncertainties will be estimated in section 6f.

6. Results

a. Surface energy balance

The daily mean SEB values for the entire period at sites 2 and 3 are presented in Fig. 10. The net radiation R, the largest positive flux in the first part, seems to decrease toward the end of the measuring period. Moreover, it varies considerably within this period, mainly due to changes in cloudiness. At site 3, the other positive term is the sensible heat flux H. Generally, in summer R is the largest positive term, whereas in winter only H heats the surface. At both sites, R becomes smaller toward the end of the period, which can be an indication of the fact that the short, peaked summer

a) SITE 2 (BLUE ICE)

b) SITE 3 (SNOW)
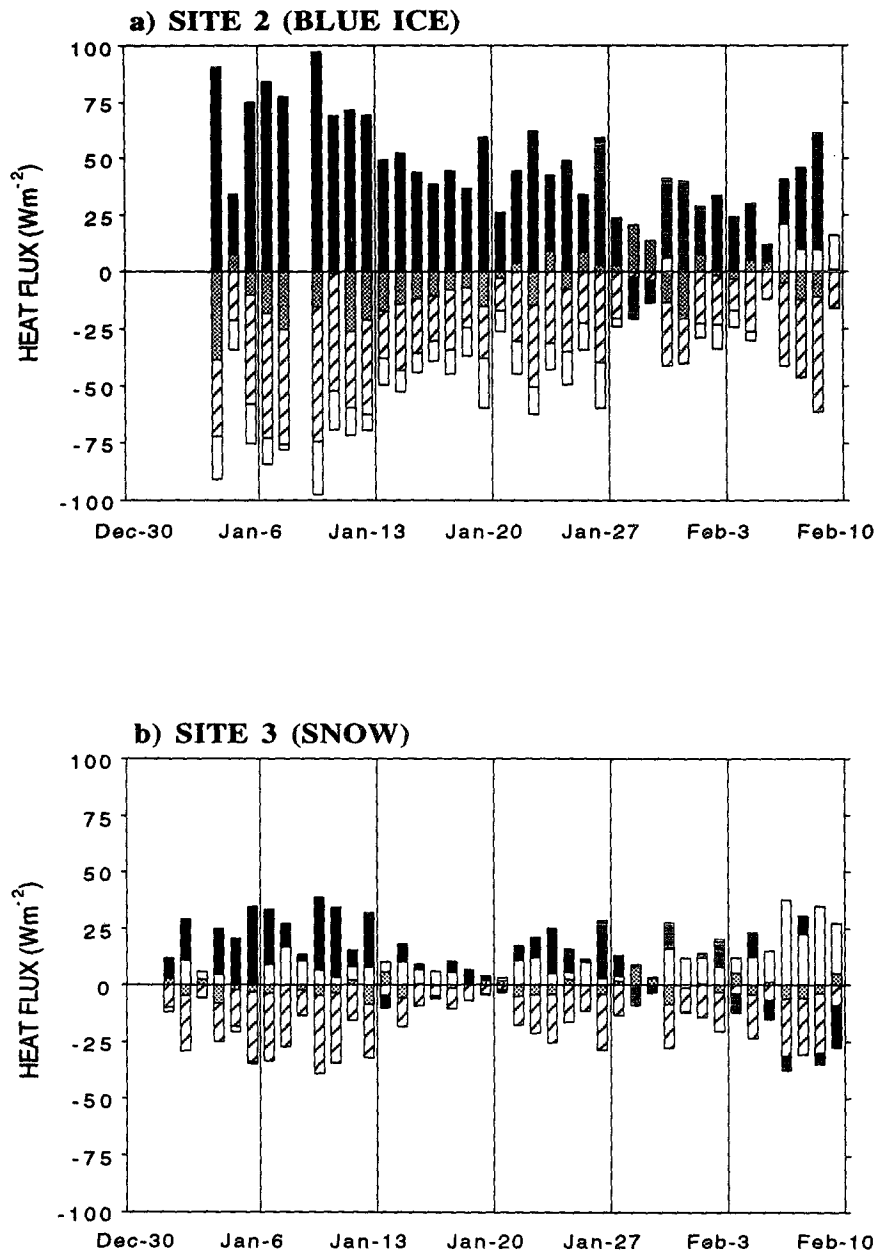
FIG. 10. Daily mean values of the energy balance terms at (a) site 2 and (b) site 3. The net radiative flux is indicated by black areas, sensible heat flux by white areas, latent heat flux by hatched areas, and the total subsurface energy flux by gray areas.

period is ending. (At site 3, H becomes even larger than R toward the end.) Most of the heat is used for sublimation (LE) at both sites. The total subsurface energy flux G is very small at site 3 and somewhat larger at site 2, which indicates that the ice gains more heat than snow during summer. The variability of the fluxes is large and clearly connected with different weather types. This will be explored in more detail in section 6e.

The mean daily cycle of the SEB terms for all sites is shown in Fig. 11. The daily cycle of all components is determined mainly by the net shortwave radiation S. The most dominant difference between ice and snow is the larger value of S for ice in daytime. The shading by mountains surrounding site 2 is apparent in the early morning. The diurnal variation in the net long-wave radiation L is dominated by variations in the emitted longwave radiation and thus in the surface
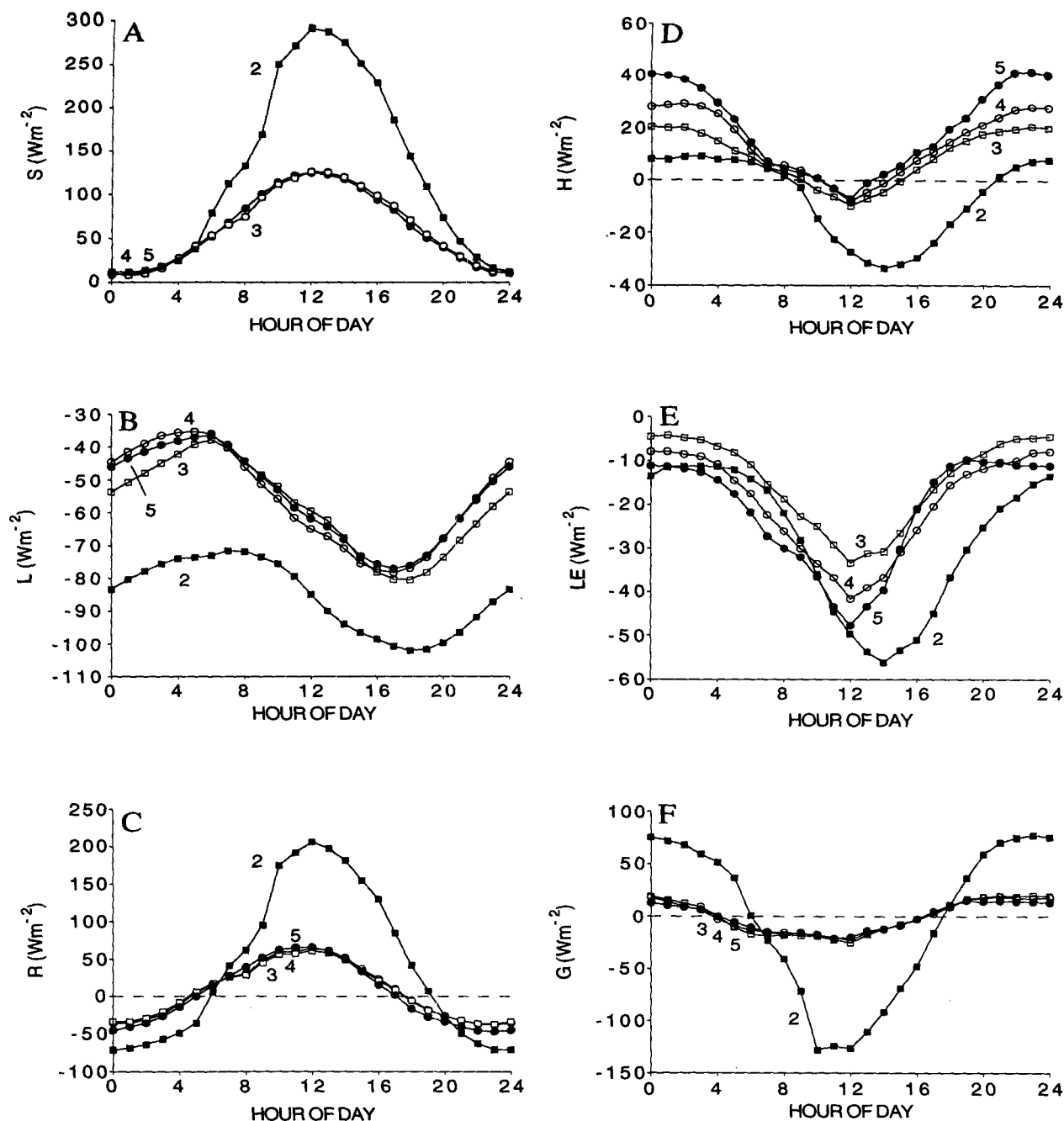
FIG. 11. Mean diurnal cycle of (a) net shortwave radiation, (b) net longwave radiation, (c) net radiation, (d) sensible heat flux, (e) latent heat flux, and (f) total subsurface energy flux at sites 2, 3, 4, and 5 for 1 January–10 February 1993.

temperature. Maximum heat loss due to L occurs around 18 h, 6 h after S is at its maximum. This can be attributed to the difference in phase between the diurnal cycle of incoming and emitted infrared radiation: $L^\uparrow$ peaks at 13 h (snow) and at 14 h (ice), whereas $L^\downarrow$ is maximum at 10 h and minimum around 20 h, in qualitative agreement with results of Wendler et al.

(1988). As a result, the net longwave radiation lags S by some hours, the phase lag being largest over ice. At night, R is negative and the surface air layer is stably stratified, as is indicated by a positive value of H. Daytime heating of the surface causes unstable conditions (negative H), lasting 13 h over ice and 3–6 h over snow. The latent heat flux is negative throughout the

day, indicating heat loss through sublimation. In the afternoon, the value of LE is comparable to L, especially at sites 2 and 5. The total energy flux into the snow/ice closely follows the diurnal behavior of R. Obviously, G_s closely follows the diurnal variation in S while G_{c_0} peaks a few hours earlier, as can be easily understood from the temperature evolution in the top layers of the snow/ice (see appendix B). The differences between the diurnal cycle of G as presented here and estimates from other studies are discussed in appendix B. The difference in amplitude of G between ice and snow reflects differences in their respective radiative (ζ and β) and conductive (K_s) characteristics. At site 2 in daytime, most of the energy is used to heat the ice. There, G is even larger (negative) than L. The diurnal heating of the ice expands deeper than for snow. At night, over ice there is a balance between G (mainly upward heat conduction) and L, which keeps the surface temperature relatively high. Hence, the stratification of the lower atmosphere remains moderately stable in contrast to snow surfaces over which the air can become very stably stratified. This is reflected by the differences in H at night. Thus, the high temperatures over ice (Fig. 5c) can be understood qualitatively from the diurnal cycle of the SEB. At site 5, the nocturnal balance is mainly between H and L, which is very typical for the Antarctic slopes with its inversion winds, in accordance with the results of Wendler et al. (1988).

The spatial variation in the turbulent fluxes from site 2 to 5 is very interesting. Figure 12 shows the friction velocity u_*, the temperature scale θ_*, and the flux Richardson number Ri_f, which is defined as (Stull 1988)

$$Ri_f = \left(\frac{g}{\theta_v}\right)\overline{(w'\theta'_v)}\left[\overline{(u'w')}\frac{\partial \bar{u}}{\partial z}\right]^{-1}, \qquad (12)$$

in which $\partial \bar{u}/\partial z$ is taken from (5a). The term $\overline{\theta_v}$ is the virtual potential temperature. The sensible heat flux increases going from site 2 to 5. Over snow, the increase is largely due to higher wind speeds (and hence u_*) outside the valley, especially at night. The fact that unstable conditions prevail for some time in the afternoon has important implications for the surface wind field, as described by Kodama et al. (1989). They showed that the change in the wind regime in the afternoon is closely connected to the SEB, as described in section 4. The difference in the H of ice and snow can be attributed mainly to variations in θ_*. At night, the sensible heat flux is small over ice and strongly positive over snow, especially at sites 4 and 5. This causes the forcing of the inversion winds to be strongest at site 5 and nearly zero at site 2. The diurnal variation of Ri_f, which is a measure of stability, is connected to the daily cycle of u_* and θ_*. At night and in the early morning, Ri_f is close to zero at site 5 through the large shear production. In daytime, the large values of θ_*
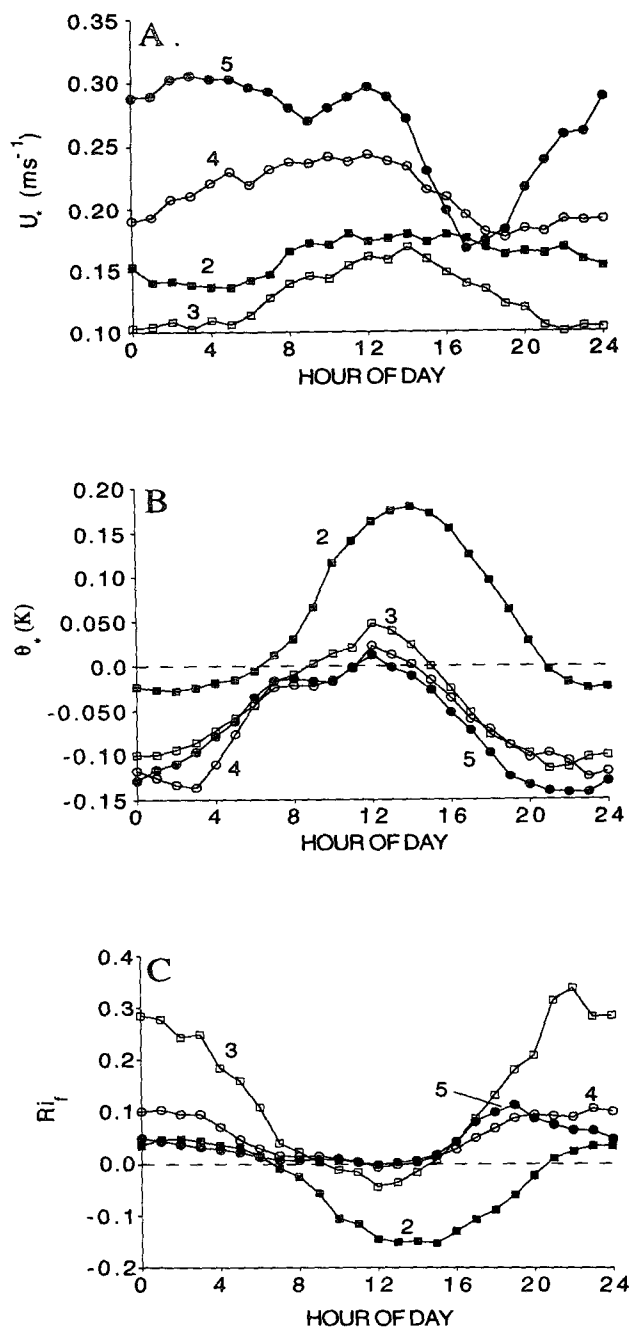
FIG. 12. Mean diurnal cycle of (a) friction velocity, (b) temperature scale, and (c) flux Richardson number at 2 m at sites 2, 3, 4, and 5 for 1 January–10 February 1993.

cause low values of Ri_f at site 2, where the most unstable conditions therefore occur.

The latent heat flux is negative everywhere, indicating an upward moisture flux. It reaches its maximum values (upward) in the afternoon. A major part of the sublimation (73%–80%) takes place when R is positive. From this it can be understood that most of the annual

sublimation takes place in the short summer, during unstable conditions in daytime (Budd 1967; Fujii and Kusunoki 1982; Clow et al. 1988).

Table 4 summarizes the period mean values of the SEB terms. The mean shortwave radiation on ice is approximately twice as large as over snow due to a doubling of the absorption fraction ($1 - \alpha_s$). Note that the albedo of snow is within the range of what is normally found. Shading by the surrounding mountains at site 2 decreases the incoming shortwave radiation by approximately 40 W m^{-2} and therefore S by 18 W m^{-2} in comparison with site 3. Variations in L are due mainly to differences in the emitted longwave radiation and hence T_s. The mean sensible heat flux is upward over ice and downward over snow. Thus, on average, the air above ice is warmed whereas it is cooled over snow. The mean sublimation rates are indeed largest over ice, as can be understood from the large moisture gradient induced by the high ice surface temperatures. However, the spatial variations over snow show that LE increases toward site 5 through the increasing wind speed (q_* is merely constant). At sites 4 and 5 the heat loss due to sublimation is approximately one-third of the heat gain through S. The subsurface energy flux G is negative upward, indicating heating of the subsurface snow/ice layers. The mean conductive heat flux G_{c_0} is positive and therefore heats the surface, while G_s is obviously downward. The larger value of G_{c_0} over ice can be explained by the larger value of K_s, which causes the deep penetration of the annual temperature wave as compared to snow.

The relative importance of the surface fluxes can be inferred from Fig. 13. The sum of the positive fluxes are scaled to 100%. Clearly, going from site 2 to 5, R decreases in importance as heat gain while H more or less replaces it. The largest heat sink everywhere is LE. At site 5, the turbulent fluxes balance each other with
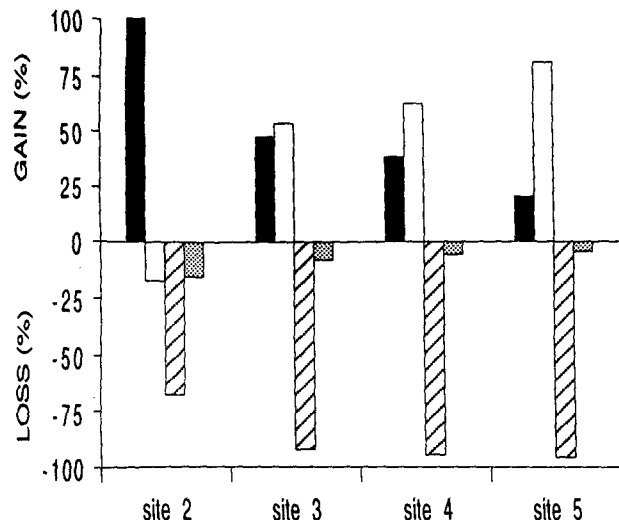

FIG. 13. Relative importance of the mean surface heat fluxes for 1 January–10 February 1993. All positive fluxes are summed and scaled to 100%. The net radiative flux is indicated by black areas, sensible heat flux by white areas, latent heat flux by hatched areas, and the total subsurface energy flux by gray areas.

a small positive contribution of R. This qualitatively resembles the SEB of an undisturbed snow field in Adelie Land (Wendler et al. 1988) at 105 km from the coast. There, the net radiation is also small compared to the magnitude of the turbulent fluxes. It is therefore concluded that the SEB at site 5 can be regarded as representative for the intermediate slopes of Antarctica in summer.

b. Subsurface temperatures

The subsurface temperatures as calculated by the model can be compared to measured values. Figure 14

TABLE 4. Mean values of the SEB components and related variables for the entire measuring period. An asterisk (*) indicates that the value was not measured locally, see Table 3.

|	Site 2	Site 3	Site 4	Site 5
Incoming shortwave (W m^{-2})	291.9	330.2	330.2*	315.3
Reflected shortwave (W m^{-2})	−164.0	−266.5	−266.5*	−252.2
Net shortwave S (W m^{-2})	127.9	63.7	63.7*	63.1
Incoming longwave (W m^{-2})	199.7	203.0	203.0*	200.4*
Emitted longwave (W m^{-2})	−285.2	−259.0	−258.5	−258.9
Net longwave L (W m^{-2})	−85.5	−56.0	−55.5	−58.5
Net radiation R (W m^{-2})	42.4	7.7	8.2	4.6
Albedo α_s	0.56	0.81	0.81*	0.80
Sensible heat flux H (W m^{-2})	−7.2	8.7	13.4	18.5
Latent heat flux LE (W m^{-2})	−28.7	−15.1	−20.4	−22.1
Conductive heat flux G_{c_0} (W m^{-2})	19.1	5.1	5.2	5.3
Penetrated solar flux G_s (W m^{-2})	−25.6	−6.4	−6.4	−6.3
Total subsurface energy flux G (W m^{-2})	−6.5	−1.3	−1.2	−1.0
Surface temperature (°C)	−7.0	−13.4	−13.4	−13.3
Friction velocity u_* (m s^{-1})	0.161	0.128	0.211	0.261
Temperature scale θ_* (K)	−0.055	0.046	0.062	0.067
Moisture scale q_* (10^{-5} kg kg^{-1})	−5.5	−2.4	−2.4	−2.3
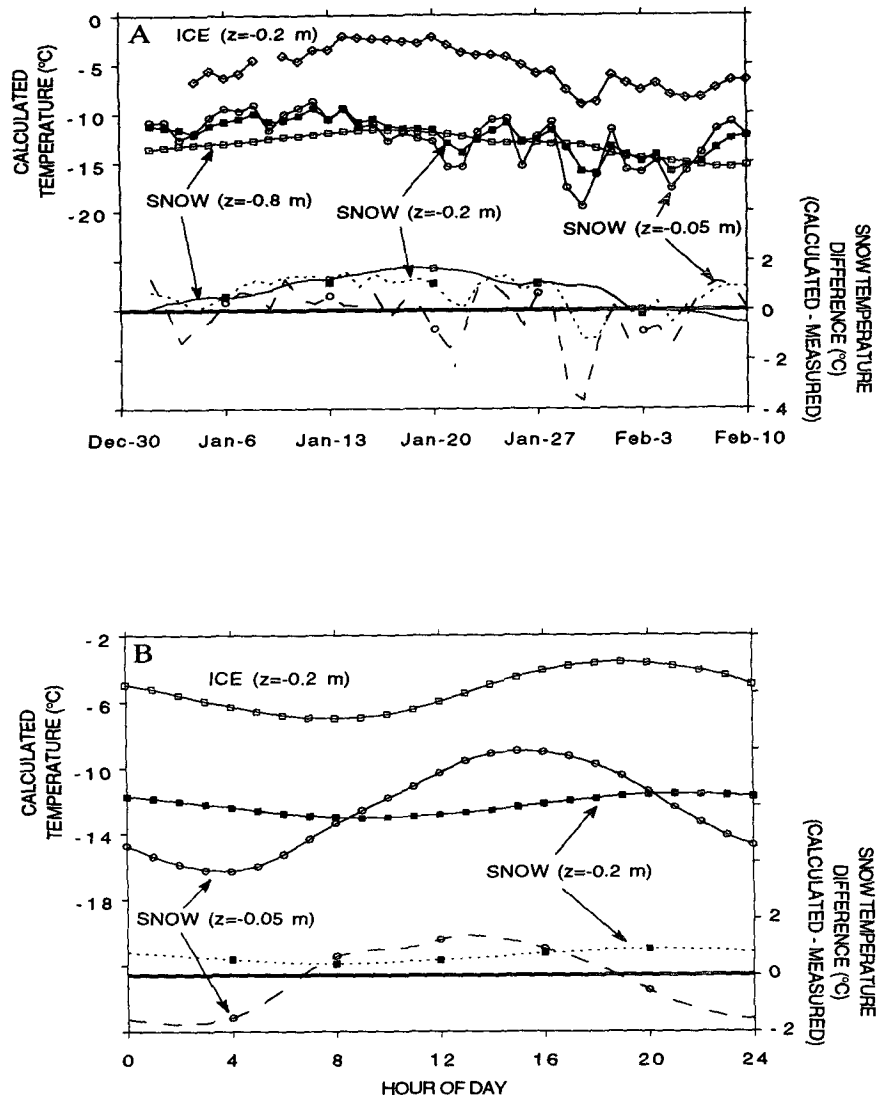
FIG. 14. (a) Calculated daily mean snow temperatures and difference between measured and calculated temperatures at three depths together with the calculated ice temperature at 20-cm depth. (b) Mean diurnal cycle of calculated snow temperature and difference between measured and calculated temperatures at two depths together with the calculated ice temperature at 20-cm depth for 1 January–10 February 1993.

shows daily mean and mean diurnal variations of calculated snow temperatures at site 3 together with the deviation from the measured snow temperatures. Except for two days, the daily mean differences remain within 2°C at all depths. The maximum errors in the daily mean temperature are $-3.8°C$ (-5 cm) and $1.9°C$ (-80 cm). The calculated temperature at -5 cm is too high in daytime and too low at night, whereas the temperature at -20 cm is too high throughout the day. The snow temperature measurements show a slight cooling in the upper 80 cm of the snowpack, equivalent to a heat flux divergence of -0.2 W m^{-2} over the entire period. For the model this is -0.7 W m^{-2}, corresponding to downward heat fluxes of 1.3 W m^{-2} at the surface

(Table 4) and 2 W m^{-2} at -80 cm (Table 3). In reality, at the end of the summer period the seasonal summer temperature wave is slowly moving downward while the surface layers are starting to cool. Therefore, the constant lower boundary flux approximation cannot be applied strictly for the whole period; as a result, the calculated cooling rates in the uppermost 80 cm of snow are slightly too high.

The ice temperature at site 2 at $z = -20$ cm is also shown in Fig. 14 for comparison. As expected, the ice is warmer than the snow, its daily amplitude larger, and its phase lag with S smaller. Paradoxically, the diurnal cycle of the temperature at some depth is larger than over snow, whereas the opposite applies to the surface temperature.
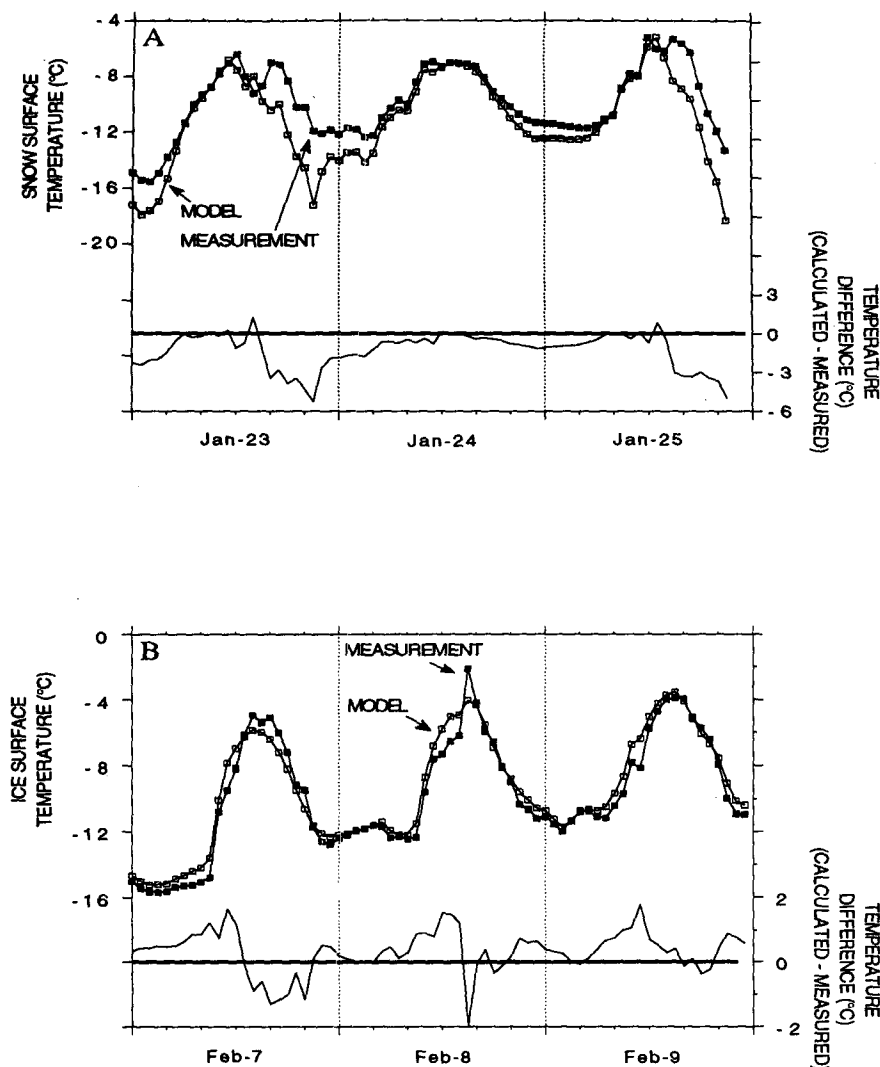
FIG. 15. Comparison of measured and calculated surface temperatures at (a) site 3 and (b) site 2. Only measurements for which the radiational errors were considered to be small have been used. The mean wind speed for the three days considered was 4.9 m s⁻¹ at site 3 (23–25 January) and 9.3 m s⁻¹ at site 2 (7–9 February).

This is due to the fact that the surface can instantaneously lose its heat through longwave radiation and turbulent exchange. Beneath the surface, however, only the slow conduction process can cool the layers. Thus, in ice the large radiative heating of the subsurface layers is counteracted only slowly by conduction, which causes the large diurnal temperature variations.

A problem that has been encountered when the model is applied over ice is that occasionally afternoon temperatures above 0°C are calculated, especially near the surface. Since surface melting was not observed at site 2 throughout the measuring period, the model somewhat overestimates near-surface heating rates. Presumably, this can be attributed either to uncertainties in the radiation measurements or to errors in cal-

culating the penetration of radiation and turbulent fluxes. However, subsurface ice melting has been observed in other BIAs, and therefore, this possibility cannot be entirely ruled out here. Brandt and Warren (1993) are able to calculate this so called "solid-state greenhouse effect" in ice, although their heating rates are clearly exaggerated due to the neglect of scattering on air bubbles. The implication of the overestimated surface temperatures at site 2 is that the turbulent fluxes and the outgoing longwave radiation are somewhat overestimated, especially in daytime.

c. Surface temperatures

As stated in section 3, on some days the surface temperature measurements at sites 2 and 3 were judged to

be accurate enough to be compared to the modeled surface temperatures. On these days, strong winds sufficiently ventilated the instruments to eliminate possible radiation errors. Figure 15 shows the observed and modeled surface temperatures on the selected days. At site 3 they agree mostly in daytime, when the wind speed is largest. At night, the differences can be considerable, presumably due to lower wind speeds that enhance the radiational errors. Over ice there seems to be much better agreement, even at night. Differences remain within 2°C, which is remarkably good considering the difficulties in the measurements and the possible inaccuracies in the modeling results described above. Although the model is tuned to do so, the fact that under these circumstances the model accurately reproduces the daily cycle of the surface temperature more than one month after initialization indicates that the calculated SEB terms may be quite accurate as well.

d. Sublimation rates

Ablation measurements were carried out near site 2 where the largest sublimation rates were expected. There, every 2–6 days a stake was measured that had been drilled into the ice during an earlier expedition. A stake near site 3 was also measured but less frequently. During the measuring period, the mean ablation at site 2 was 0.94 mm w.e. per day, which is less than in earlier years (Jonsson 1992). The cumulative measured mass balance and the cumulative calculated sublimation rates for sites 2 and 3 are shown in Fig. 16. As expected, the ablation rate decreases somewhat toward the end of the measuring period since the sublimation rates peak in the summer season (Fujii and Kusunoki 1982; Jonsson 1992). The calculated values seem to agree well with the measurements for site 2 although the total calculated sublimation rate is approximately 10% smaller than the total measured ablation. At site 3, the mass balance over the measuring period is almost zero, which suggests that site 3 is located near the equilibrium line. The importance of snowdrift processes in the surface mass balance over snow can be inferred from the stake readings at site 3, which indicate deposition of snow during the periods 3–8 January and 25 January–1 February and erosion during the period 8–12 January.

Figure 17 shows the calculated ablation rates against the measured ablation rates for each 2–6-day period for site 2. The agreement seems reasonable although significant deviation occurs for some periods. Presumably, these deviations can be attributed mainly to uncertainties in the stake measurements. As stated earlier, surface melting is expected to be of minor importance, although the calculated surface temperatures sometimes rise above 0°C in the afternoon. Ablation is therefore expected to be due entirely to sublimation. It is concluded that simulated and measured sublimation rates compare reasonably well at site 2, which gives credit to the model-derived SEB terms.

e. Surface energy balance terms for three predominant weather regimes

To study the variability of the SEB during summer, three weather regimes are distinguished that are expected to be connected to distinctly different SEB regimes. With respect to temporal variations in latent heat flux (LE), this will give insight into which weather regime is associated with the highest sublimation rates and therefore is most favorable for the maintenance of BIAs. A clear distinction can be made, especially inside the valley, and therefore the following criteria are applied to the conditions at site 3.

1) Predominantly weak westerly winds are present throughout the day together with small amounts of clouds (mainly altocumulus and cirrus). At night, the weak large-scale flow allows the formation of shallow katabatic layers (10–20-m depth) that enter the valley down the local slopes.

2) Equal to type 1 except that between 9 and 12 h the wind direction becomes easterly and the wind speed increases rapidly. Adiabatically warmed air replaces the cold stagnant air inside the valley in a front-passage-like behavior. Probably, the entrainment at the top of the basin becomes large due to vigorous mixing in daytime. Momentum, warm and moist air then mixes downward to the surface. In most cases, this phenomenon stops when the radiation balance becomes negative and, consequently, mixing is suppressed.

3) Strong easterly winds associated with an enhanced katabatic wind due to coastal cyclonic activity occur. Large amounts of frontal clouds (mainly stratus, altostratus, and nimbostratus) allow for some precipitation. The fierce winds cause drifting and blowing snow.

A total of 41 days (1 January–10 February) were used. Two days could not be categorized in one of the three regimes since during these days a transition took place between two regimes. Table 5 lists some characteristics of the three weather regimes for sites 3 and 5. Type 3 is characterized by relatively warm and moist conditions, although the differences in mean temperature and humidity are not large. Note the low directional constancy for type 1 inside the valley as opposed to site 5. The variability of the surface wind regime is largest inside the valley. The different conditions at site 5 for the three weather regimes presumably reflect the regular (undisturbed) variability of the summertime meteorological conditions of the Ritscherflya plateau.

The SEB terms for the three regimes for sites 2, 3, and 5 are summarized in Tables 6–8 as deviations from the mean values. The variations of the surface fluxes can be explained largely from the variations in cloudiness and wind speed (Table 5). Type 1 is characterized by high S and a much lower L, which reduces the net radiation. The lower wind speeds result in smaller turbulent fluxes. The snow layers at sites 3 and 5 are cooled
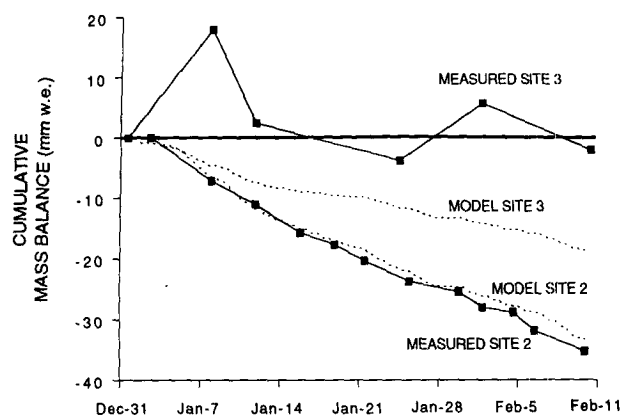
FIG. 16. The cumulative calculated sublimation rate and measured mass balance from stake readings for sites 2 and 3.

FIG. 17. Comparison of calculated and measured mass balance values for 11 periods of 2–6 days at site 2. Also shown is the 1:1 line.

while the warming of the ice at site 2 is largely reduced. The characteristics of type 2 are the larger net radiation as compared with type 1 due to more (low) clouds and higher surface temperatures together with larger turbulent fluxes due to a larger wind speed. The surface fluxes are largest for type 3; this can be attributed to the large amount of clouds and the highest wind speeds.

The influence of cloudiness on the radiation balance over high reflective surfaces has received much attention. The observation of an increasing net radiation resulting from increasing cloudiness led to the term "radiation paradox" (Ambach 1974; Wendler 1986). It is caused by an increase in the net longwave radiation with increasing cloudiness that is larger than the decrease in net shortwave radiation, as can be inferred from Tables 6–8. However, other effects, such as wind speed and precipitation that correlate with variations in cloudiness will also influence the radiation balance. To illustrate the radiation paradox over snow, the daily mean net radiation R as a function of total cloud amount N at site 3 is given in Fig. 18. Although the scatter is large, it is clear that R increases with cloudiness, the linear regression on the data being $R = -1.2 + 25.0N$. The increase of 25 W m^{-2} from clear sky to overcast conditions is in good agreement with results of Wendler (1986).

The variation of H and LE between the various circulation types deserves more attention. The specific humidity profile in the surface layer is always strongly unstable, indicating an upward moisture flux. Thus, variations in LE at a specific location are determined largely by differences in wind speed and to a lesser extent by variations in stability and moisture gradient. On the other hand, H depends critically on stability and wind speed. When wind speed increases, u_*, and therefore H, will be larger. However, a higher wind speed makes the stratification more neutral, decreasing θ_* and H. As a result, variations in H are less pronounced. This subtle balance hampers the understanding of the sign of change in H for each weather regime. Clearly, the variations in H for the three circulation types are smaller than in LE. Thus, the variability in the summertime SEB is restricted mainly to R and LE, especially at sites 2 and 5.

The surface winds outside the valley are of katabatic nature for type 1, although their strength is decreased. This is consistent with the large value of H, indicating that the forcing mechanism of inversion winds is still present. The wind climate inside the valley shows katabatic characteristics for type 3 in which the turbulent exchange remains high even at night. Sublimation rates

TABLE 5. Mean characteristics of the three weather regimes for sites 3 and 5 for the period 1 January–10 February.

Regime	Number of days	Cloud amount (tenths)	Wind speed (m s^{-1}) 6 m		Temperature (°C) 2 m		Directional constancy 6 m		Specific humidity (g kg^{-1}) 2 m
			Site 3	Site 5	Site 3	Site 5	Site 3	Site 5	Site 3
1	11	1.7	2.0	4.1	−10.8	−12.1	0.39	0.86	1.05
2	11	1.9	4.0	6.5	−9.7	−12.3	0.65	0.92	1.00
3	17	6.1	6.0	7.1	−9.7	−11.3	0.87	0.93	1.14
Mean	41	3.6	4.3	6.1	−9.9	−11.6	0.64	0.91	1.08

TABLE 6. Change in SEB components (W m^{-2}) with respect to the mean values for site 2 for the three weather regimes. A positive change indicates additional flux toward the surface.

	Regime 1	Regime 2	Regime 3
S	10.6	10.4	−11.2
L	−30.4	−13.5	23.2
H	0.1	1.0	−0.6
LE	15.2	1.6	−8.9
G	4.5	0.5	−2.5

TABLE 8. As in Table 6 except for site 5.

	Regime 1	Regime 2	Regime 3
S	7.0	5.2	−8.5
L	−21.1	−2.9	16.8
H	−0.9	2.4	−1.0
LE	12.1	−4.0	−5.6
G	2.9	−0.7	−1.7

are largest for type 3, where the additional radiation is transferred mainly into energy loss by LE, although this is counteracted by the inland moisture advection, reducing the vertical moisture gradient and therefore the sublimation rate. The spatial variation of LE has important implications for the mass balance. The fact that variations in LE are larger over ice than over snow indicates that the existence of the BIA has some feedback on the mass balance.

f. Influence of measuring errors and model assumptions on the SEB

To quantify the model's sensitivity to applied assumptions and uncertainties in measured input values, these parameters are varied around their applied standard values. The resulting changes in SEB components are listed in Tables 9 (site 2) and 10 (site 5). The values at site 3 are comparable to those at site 5. Only the parameter changes are considered for which the SEB components significantly differed from the standard run. The most relevant ones will be discussed below.

Obviously, over snow the turbulent fluxes increase (absolute) if the z_{0h} and z_{0q} are increased. Over ice the turbulent fluxes cool the surface. An increase in z_{0h} and z_{0q} will therefore lead to a lower surface temperature. Accordingly, the increase in the turbulent fluxes is suppressed and other fluxes (e.g., $L^{\uparrow}$) change as well. According to Brutsaert (1982), z_{0h} and z_{0q} are somewhat larger than z_{0m} over smooth surfaces (sites 2 and 3) and smaller than z_{0m} over aerodynamically rough surfaces (sites 4 and 5). Garratt and Hicks (1973) summarize experimentally derived roughness lengths and conclude that z_{0h} and z_{0q} do not deviate from z_{0m} by more than one order of magnitude for roughness Reynolds number (Re $= u_* z_{0m} / \nu$) ranging from 10^{-1}

TABLE 7. As in Table 6 except for site 3.

	Regime 1	Regime 2	Regime 3
S	6.6	6.6	−8.5
L	−17.1	−5.8	14.9
H	−5.0	1.9	2.0
LE	11.1	−0.3	−7.0
G	4.4	−2.4	−1.4

to 10^2 (which is the range under consideration). Increasing the scalar roughness lengths by a factor of 10 at site 2 and decreasing them by a factor of 10 at site 5 yields a maximum absolute increase (site 2) or decrease (site 5) in the turbulent fluxes of 4.5 W m^{-2}. (At site 2 this would mean that the calculated sublimation closely matches measured ablation.) The surface temperatures will then be significantly lower, especially in the afternoon when changes in LE are at their maximum.

Increasing the momentum roughness length z_{0m} by one order of magnitude also yields larger (absolute) turbulent fluxes. At site 2, where the mean H and LE are both upward directed, the surface temperature decreases and hence L increases. The turbulent shear production is most important at site 5, as can be inferred from the relative large change in H and LE for a tenfold increase in z_{0m}.

Obviously, increasing the amount of radiation leads to higher surface temperatures and therefore to an increase in the longwave emitted radiation, the upward turbulent fluxes and downward conductive heat flux. A decrease in the parameter determining the penetration of shortwave radiation (ζ) leads to lower surface temperatures. More radiative energy is then transferred to deeper snow–ice layers (larger absolute G), thereby raising subsurface temperatures, which then deviate
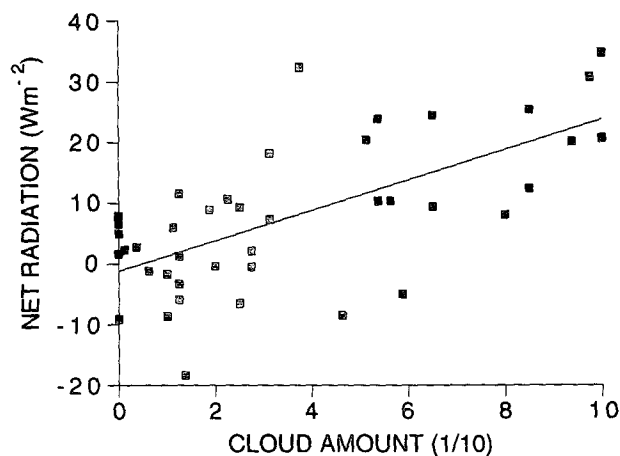

FIG. 18. Daily mean values of net radiation as a function of total cloud amount for site 3. The line is the linear regression to the data, whose coefficients are given in the text.

TABLE 9. Change in the mean surface energy fluxes (W m^{-2}) and surface temperature (°C) as a result of varying input parameters for site 2.

	S	L	H	LE	G	T_S
$z_{0m} = 0.07$ mm	0.0	1.6	1.8	−3.7	0.3	−0.3
$z_{0h} = z_{0q} = 0.07$ mm	0.0	2.1	1.8	−4.3	0.4	−0.5
$L_{corr} = 15$ W m^{-2}	0.0	3.5	−1.8	−1.3	−0.4	0.4
$S + 2\%$	2.4	−0.7	−0.8	−0.7	−0.2	0.2
$\zeta = 0.7$	0.0	0.5	1.0	1.0	−2.5	−0.1
$T_{init} = -4°C$	0.0	−1.3	−1.6	−1.2	4.1	0.3
Atmospheric temperature + 0.2°C	0.0	−0.4	0.8	0.0	−0.4	0.1
Relative humidity +2%	0.0	−0.2	−0.3	0.6	−0.1	0.1
Wind speed + 0.2 m s^{-1}	0.0	0.3	0.2	−0.6	0.1	−0.1

more from the measured values. Considering the impact of a 0.1 decrease in ζ on the radiation balance of the surface, the resulting increase in the other fluxes is relatively small. The direct change in surface temperature caused by a change in ζ is partially offset by indirect heating from subsurface layers adjacent to the surface layer (where most of the additional radiative energy is absorbed).

If the relative humidity at site 5 is decreased by 7.5% (i.e., equal to site 3), the latent heat flux increases by 3.9 W m^{-2} ($\approx 18\%$). This shows that the simulated sublimation rates are not very sensitive to the exact relative humidity at site 5.

The effect of changing the initial temperature profile to −4°C in ice yields relatively small changes in the SEB. It is only the value of G that increases significantly due to a larger upward conductive flux, which implies that the ice loses its "extra" internal energy to the atmosphere. The mean surface temperature is only slightly higher.

The uncertainties in the SEB results due to measuring inaccuracies in air temperature (±0.2°C), relative humidity (±2%), and wind speed (±0.2 m s^{-1}) are small (<1.2 W m^{-2}) compared to SEB changes resulting from the assumptions made. However, note that if the turbulent fluxes are evaluated from gradients between two levels in the atmosphere, errors in H and LE can become significantly larger.

From this section it can be concluded that the SEB as presented in section 6a will not be subject to major changes due to measurement errors and/or uncertainties in the model assumptions. Therefore, the SEB results seem to be quite robust. It should be noted that the parameters not treated here (e.g., K_s and G_{-H_d}), although not seriously influencing the SEB, can lead to significant changes in the vertical and temporal distribution of the subsurface temperatures.

7. Discussion and conclusions

A detailed analysis of the variations in the SEB along a straight line in the valley Scharffenbergbotnen in which a large BIA is located is presented. In this manner, differences between blue ice and snow could be studied. A simple model was used to evaluate the terms of the SEB that were not measured directly. A comparison of modeled and measured snow temperatures (site 3), surface temperatures (sites 2 and 3), and sublimation rates (site 2) indicates that, after some tuning, the model provides a fairly accurate simulation of the SEB and subsurface temperatures.

At the three sites over snow, the SEB remains qualitatively constant, although large variations occur in the magnitude of the individual fluxes. These variations depend largely on the location: outside the valley the SEB interacts with the large-scale surface wind field, whereas inside the valley the surface flow seems to be more or less decoupled from this large-scale flow resulting in low wind speeds and, consequently, smaller turbulent fluxes.

TABLE 10. As in Table 9 except for site 5.

	S	L	H	LE	G	T_S
$z_{0m} = 7.5$ mm	0.0	−0.3	8.7	−8.5	0.1	0.1
$z_{0h} = z_{0q} = 0.075$ mm	0.0	−0.1	−4.2	4.4	−0.1	0.0
$L_{corr} = 25$ W m^{-2}	0.0	4.0	−2.7	−1.2	−0.2	0.2
$S + 2\%$	1.2	−0.3	−0.6	−0.3	−0.0	0.1
$\zeta = 0.8$	0.0	0.4	0.7	0.5	−1.6	−0.1
Atmospheric temperature + 0.2°C	0.0	−0.5	1.1	0.1	−0.7	0.1
Relative humidity − 7.5%	0.0	0.8	3.0	−3.9	0.1	−0.2
Relative humidity + 2%	0.0	−0.2	−0.9	1.1	0.0	0.0
Wind speed + 0.2 m s^{-1}	0.0	−0.1	0.9	−0.8	0.0	0.0

The largest spatial differences in SEB occur between blue ice and snow. The most important divergent characteristics of blue ice as compared to snow are

- lower albedo (0.56 versus 0.80),
- larger thermal conductivity coefficient,
- smaller extinction coefficient for penetrating solar radiation, and
- lower roughness length of momentum.

These different characteristics lead to distinct differences between the SEB terms of blue ice and of snow.

- Larger absorption of shortwave radiation of ice in daytime.
- Higher surface and subsurface temperatures of ice, which causes more unstable conditions in daytime and a larger heat loss by longwave radiation.
- Larger energy flux into the ice due to its larger thermal conductivity and its smaller radiative extinction coefficient. At night, the energy flux in the ice is directed upward and heats the surface layers.
- An average upward-directed sensible heat flux over ice as compared to a downward one over snow. This is due to more unstable conditions in daytime and less stable conditions at night over ice. Thus, the forcing mechanism of inversion winds (i.e., cooling of the surface air layer) is present over snow and severely reduced over ice.
- The latent heat flux is more negative over ice due to more unstable conditions in daytime, indicating greater mass loss through sublimation.

The SEB can effectively be characterized by the net radiation and turbulent fluxes. Therefore, these are plotted in Fig. 19 for the sites 2, 3, and 5, as well as for snow surfaces at some other locations in the vicinity of the escarpment region. The characteristic variability in the summertime SEB is shown by the three dots that indicate the values for the different weather regimes described in section 6e. Snow surfaces show up in the lower right corner of the plot: they are characterized by relatively small fluxes, whereas over blue ice the fluxes are much larger. It should be noted that the variability in the turbulent fluxes is due mainly to variations in the latent heat flux. The SEB over snow seems to be comparable to the SEB of the other locations plotted in Fig. 19. As discussed earlier, the fluxes over blue ice display a much larger variability. More SEB studies on other BIAs are needed for comparison with the site 2 results.

The horizontal extent of a BIA is determined by the spatial mass balance gradient. An important element of the surface mass balance on Antarctica is the mass loss through sublimation. The factors that mainly control the spatial variability of the latent heat flux in the vicinity of a BIA are the following.

- High surface temperatures of ice (mainly due to its lower albedo compared to snow), causing more un-
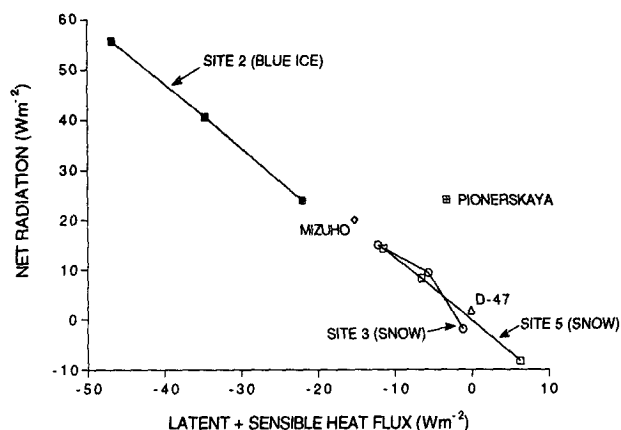
FIG. 19. The summertime surface energy balance characterized by the net radiation and the turbulent fluxes for sites 2, 3, and 5. The three dots are values for the three circulation types and indicate the variability of the energy balance. Midsummer values for the snow surfaces at Mizuho in 1980 (Ohata et al. 1985), Pionerskaya in 1958 (Schlatter 1972), and D-47 in 1985 (Wendler et al. 1988), all located more or less near the intermediate slope of Antarctica, are given for comparison.

stable conditions and a larger vertical moisture gradient.

- Smaller aerodynamic roughness of ice causing smaller sublimation rates. It is unclear whether the scalar roughness lengths behave in the same way.
- Lower wind speeds inside the valley causing smaller latent heat fluxes. However, this factor is interrelated with the presence of more unstable conditions over ice.

These differences result in sublimation rates that are only 30% larger over ice (site 2) than over snow outside the valley (site 5). Since the sublimation is largest in summer, the annual mean spatial sublimation gradient is expected to be of the same order of magnitude. Obviously, the observed mass balance difference of approximately 34 cm w.e. between sites 2 and 5 cannot be explained by the sublimation gradient alone. Therefore, the accumulation gradient seems to be the most important factor controlling the extent of BIAs. Since the accumulation rate is determined mainly by the divergence of drifting snow, the accumulation gradient is likely to be determined largely by the distinct differences in wind climate in and outside the valley.

points that enabled us to improve the paper. Financial support was provided by the Netherlands Antarctic Research Programme (GOA) and the Dutch National Research Programme on Global Air Pollution and Climate Change (NOP).

APPENDIX A

Determination of the Thermal Conductivity of Snow from Subsurface Snow Temperature Measurements

At site 3, where snow temperatures were measured at five levels (-5, -10, -20, -40, and -80 cm), three methods can be used to estimate the value of the thermal conductivity K_s. The first two methods concern the vertical variation of amplitude and phase lag of the diurnal temperature cycle. If the absorption of radiation below $z = -5$ cm is neglected and a sinusoidal temperature diurnal cycle at 5-cm depth is assumed with amplitude A_0 and frequency ω, the amplitude A_z and phase lag F_z at level z are easily calculated analytically from Eq. (2) (Pal Ayra 1988):

$$A_z = A_0 \exp\left(\frac{z}{d}\right)$$

$$F_z = -\frac{z}{d} \qquad (A1)$$

with $d = (2K_s/\rho c_p \omega)^{1/2}$.

It is assumed here that K_s is constant with depth since the snow density ($= 400$ kg m^{-3}) appeared to hardly vary with depth. Seven days were chosen during which the diurnal temperature variation at 5-cm depth was approximately sinusoidal. From the regression lines in Figs. A1 and A2, the value of K_s can be calculated. The measurements at -80 cm were not used

FIG. A1. Variation of the amplitude of the diurnal cycle of snow temperature at site 3 with depth. Also shown is the linear regression to the data from which the snow thermal conductivity K_s can be calculated.

FIG. A2. As in Fig. A1 except for the phase lag.

since the daily cycle was hardly recognizable at that depth. Errors in the measuring depths and snow density are the main causes of the resulting error in K_s.

The third method is to relate the rate of energy change of the snowpack to the conductive heat fluxes at the top and bottom boundaries:

$$\rho c_p \int\int \frac{\partial T}{\partial t}\, dz dt = K_s \int \left(\frac{\partial T}{\partial z}\bigg|_{\text{top}} - \frac{\partial T}{\partial z}\bigg|_{\text{bottom}}\right) dt.$$

$$(A2)$$

The conductive heat fluxes are calculated from temperature differences between 5 and 10 cm (top) and 40 and 80 cm (bottom). These necessary approximations lead to relatively large uncertainties in the value obtained for K_s. The highest accuracy is obtained by integrating over the entire measuring period, since then the change in energy storage is significant. In Table A1, the derived K_s values are presented and compared with those obtained from empirical fits in the literature. The values obtained here seem to be somewhat lower than the values listed in the literature. For the SEB calculations, a value of 0.25 W m^{-1} K^{-1} is used for snow.

TABLE A1. Values for the thermal conductivity K_s of snow as estimated from the amplitude, phase, and energy method, together with some values from literature for a density of 400 ± 20 kg m^{-3}.

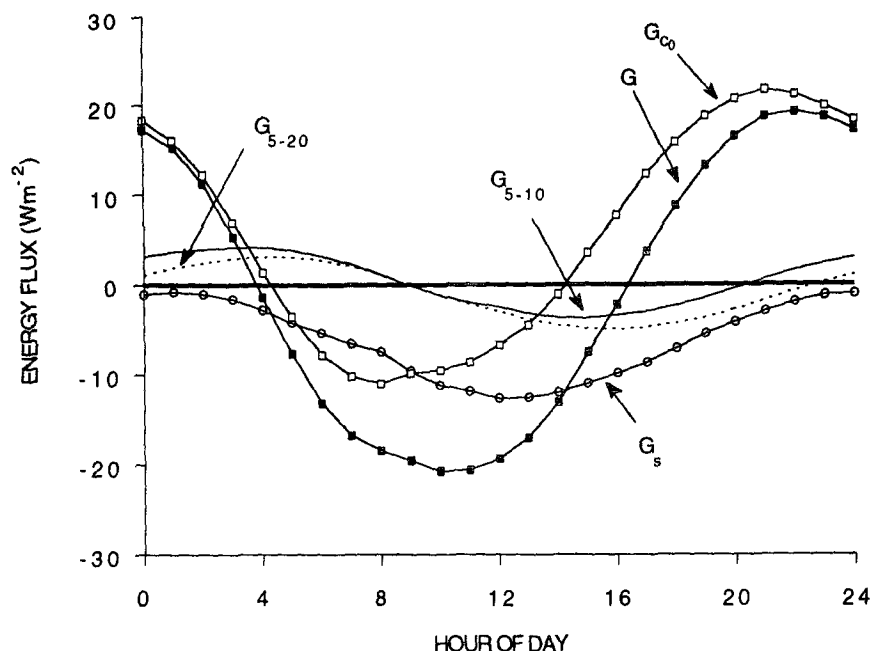|	K_s (W m^{-1} K^{-1})
Amplitude	0.23 ± 0.03
Phase	0.30 ± 0.03
Energy	0.23 ± 0.05
Paterson (1981)	0.33 ± 0.03
Anderson*	0.42 ± 0.04
Yen*	0.40 ± 0.04

* Empirical relation listed in Paterson (1981).

FIG. B1. Mean diurnal cycle of the total subsurface energy flux (G), conductive heat flux (G_{c_0}), penetrating solar flux (G_s), and the heat flux calculated from temperature differences between -5 and -10 cm (G_{5-10}) and between -5 and -20 cm (G_{5-20}) for 1 January–10 February 1993. For the calculation of the fluxes G_{5-10} and G_{5-20}, a value of $K_s = 0.25$ W m^{-1} K^{-1} was used.

APPENDIX B

Comparison of the Calculated Surface Energy Flux into the Snow with Other Methods

In Fig. B1, the mean diurnal cycle of the components of the surface energy flux into the snow, G (total), G_s (penetrating solar radiation), and G_{c_0} (conduction), at site 3 are presented. Clearly, G_s lags behind G_{c_0} for some hours, which can be understood from simple theoretical calculations (Budd 1967). The penetrating solar radiation G_s is in phase with the net shortwave radiation, whereas G_{c_0} peaks earlier due to the fact that in the morning the surface heats quickly while the adjacent subsurface layers warm slowly. Thus, the total subsurface energy flux at the surface reaches its minimum (upward) before the shortwave radiation. The phase lag between the diurnal cycle of the total subsurface energy flux at some depth and G increases with increasing depth. If the mean heat storage in the snow is small, the heat gain by radiation and conduction in daytime can be counteracted only by an upward conductive flux at night, which produces the asymmetric behavior of G_{c_0} (mean upward).

In related studies, temperature measurements from two depths sufficiently far from the surface to prevent radiational heating of the sensors are often used to evaluate G (e.g., Wendler et al. 1988). Two examples are depicted in Fig. B1 (G_{5-10} and G_{5-20}) using measured snow temperature differences between 5- and 10-cm and 5- and 20-cm depths, respectively, and K_s

$= 0.25$ W m^{-1} K^{-1}. Indeed, the expected time lag is present. Very large vertical temperature variations in the upper 20 cm of the snow deck result in strong vertical gradients in G close to the surface. As a result, the amplitude of the diurnal cycle of G_{5-10} and G_{5-20} is small compared to G. Therefore, it is concluded that this widely used approximation to estimate G is unable to produce a realistic phase and amplitude of the diurnal cycle.

REFERENCES

Ambach, W., 1974: The influence of cloudiness on the net radiation balance of a snow surface with high albedo. *J. Glaciol.,* 13(67), 73–84.

Bintanja, R., M. R. van den Broeke, and M. J. Portanger, 1993: A meteorological and glaciological experiment on a blue ice area in the Heimefront Range, Queen Maud Land, Antarctica. Svea Field Report, 29 pp. [Available from the Institute for Marine and Atmospheric Research Utrecht, Utrecht University, P.O. Box 80005, 3508 TA, Utrecht, the Netherlands.]

Brandt, R. E., and S. G. Warren, 1993: Solar-heating rates and temperature profiles in Antarctic snow and ice. *J. Glaciol.,* 39, 99–110.

Brutsaert, W. H., 1982: *Evaporation into the Atmosphere.* Reidel, 299 pp.

Budd, W., 1967: Ablation from an Antarctic ice surface. *Physics of Snow and Ice,* H. Oura, Ed., Bunyeido Printing Co., 431–446.

Carroll, J. J., 1982: Long-term means and short-term variability of the surface energy balance components at the South Pole. *J. Geophys. Res.,* 87, 4277–4286.

Clow, G. D., C. P. McKay, G. M. Simmons Jr., and R. A. Wharton Jr., 1988: Climatological observations and predicted sublimation rates at Lake Hoare, Antarctica. *J. Climate,* 1, 715–728.

Duynkerke, P. G., 1991: Radiation fog: A comparison of model simulation with detailed observations. *Mon. Wea. Rev.*, **119**, 324–341.

Dyer, A. J., 1974: A review of flux-profile relationships. *Bound.-Layer Meteor.*, **7**, 363–372.

Fujii, Y., and K. Kusunoki, 1982: The role of sublimation and condensation in the formation of ice sheet surface at Mizuho Station, Antarctica. *J. Geophys. Res.*, **87**, 4293–4300.

Garratt, J. R., and B. B. Hicks, 1973: Momentum, heat and water vapour transfer to and from natural and artificial surfaces. *Quart. J. Roy. Meteor. Soc.*, **99**, 680–687.

Greuell, W., and J. Oerlemans, 1989: The evolution of the englacial temperature distribution in the superimposed ice zone of a polar ice cap during a summer season. *Glacier Fluctuations and Climatic Change*, J. Oerlemans, Ed., Kluwer Academic, 289–304.

Herzfeld, U. C., and P. Holmlund, 1990: Geostatics in glaciology: Implications of a study of Scharffenbergbotnen, Dronning Maud Land, East Antarctica. *Ann. Glaciol.*, **14**, 107–110.

Högström, U., 1988: Non-dimensional wind and temperature profiles in the atmospheric surface layer: A re-evaluation. *Bound.-Layer Meteor.*, **42**, 55–78.

Jonsson, S., 1992: Local climate and mass balance of a blue-ice area in Western Dronning Maud Land, Antarctica. *Zeitschrift für Gletscherkunde und Glazialgeologie*, **27**, 11–29.

Kimball, B. A., S. B. Idso, and J. K. Aase, 1982: A model of thermal radiation from partly cloudy and overcast skies. *Water Resour. Res.*, **18**(4), 931–936.

King, J. C., 1990: Some measurements of turbulence over an Antarctic ice shelf. *Quart. J. Roy. Meteor. Soc.*, **116**, 379–400.

Knap, W. H., 1992: A study on the albedo and energy balance of an alpine snow field in the winter season. I.M.A.U. Rep. Vg2-12, 68 pp. [Available from Institute for Marine and Atmospheric Research Utrecht, Utrecht University, P.O. Box 80005, 3508 TA, Utrecht, the Netherlands.]

Kodama, Y., G. Wendler, and N. Ishikawa, 1989: The diurnal variation of the boundary layer in summer in Adelie Land, Eastern Antarctica. *J. Appl. Meteor.*, **28**, 16–24.

Kondo, J., and H. Yamazawa, 1986: Bulk transfer coefficient over a snow surface. *Bound.-Layer Meteor.*, **34**, 123–135.

Lunde, T., 1961: On the snow accumulation in Dronning Maud Land. *Skr. Nor. Polarinst.*, **123**, 48 pp.

Oerlemans, J., and H. F. Vugts, 1993: A meteorological experiment in the melting zone of the Greenland ice sheet. *Bull. Amer. Meteor. Soc.*, **74**, 355–365.

Ohata, T., N. Ishikawa, S. Kobayashi, and S. Kawaguchi, 1985: Heat balance at the snow surface in a katabatic wind zone, East Antarctica. *Ann. Glaciol.*, **6**, 174–177.

Orheim, O., and B. Lucchitta, 1990: Investigating climate change by digital analysis of blue ice extent on satellite images of Antarctica. *Ann. Glaciol.*, **14**, 211–215.

Pal Ayra, S., 1988: *Introduction to Micrometeorology*. Academic Press, 307 pp.

Parish, T. R., and K. T. Waight, 1987: The forcing of Antarctic katabatic winds. *Mon. Wea. Rev.*, **115**, 2214–2226.

Paterson, W. S. B., 1981: *The Physics of Glaciers*. Pergamon, 380 pp.

Schlatter, T. W., 1972: The local surface energy balance and subsurface temperature regime in Antarctica. *J. Appl. Meteor.*, **11**, 1048–1062.

Schwerdtfeger, W., 1970: The climate of the Antarctic. *World Survey of Climatology*, H. E. Landsberg, Ed., Elsevier, 253–355.

Schytt, V., 1961: Blue ice fields, moraine features and glacier fluctuations. Norwegian–British–Swedish Antarctic Expedition 1949–52. Scientific Results, Vol. IV: E. Norsk Polarinstitutt, 24 pp.

Sorbjan, Z., Y. Kodama, and G. Wendler, 1986: Observational study of the atmospheric boundary layer over Antarctica. *J. Climate Appl. Meteor.*, **25**, 641–651.

Stull, R. B., 1988: *An Introduction to Boundary Layer Meteorology*. Kluwer Academic, 666 pp.

Takahashi, S., R. Naruse, N. Masayoshi, and S. Mae, 1988: A bare ice field in East Queen Maud Land, Antarctica, caused by horizontal divergence of drifting snow. *Ann. Glaciol.*, **11**, 156–160.

Van Autenboer, T., 1964: The geomorphology and glacial geology of the Sör-Rondane, Dronning Maud Land. *Antarctic Geology*, R. J. Adie, Ed., North-Holland, 81–103.

Weller, G., 1980: Spatial and temporal variations in the South Polar surface energy balance. *Mon. Wea. Rev.*, **108**, 2006–2014.

Wendler, G., 1986: The "Radiation Paradox" on the slopes of the Antarctic continent. *Polarforschung*, **56**(1/2), 33–41.

——, 1989: On the blowing snow in Adelie Land, Eastern Antarctica. *Glacier Fluctuations and Climatic Change*, J. Oerlemans, Ed., Kluwer Academic, 261–280.

——, N. Ishikawa, and Y. Kodama, 1988: The heat balance of the icy slope of Adelie Land, Eastern Antarctica. *J. Appl. Meteor.*, **27**, 52–65.

Wiscombe, W. J., and S. G. Warren, 1980: A model for the spectral albedo of snow. I: Pure snow. *J. Atmos. Sci.*, **37**, 2712–2733.

Worsfold, R. J., 1967: Physiography and glacial geomorphology of Heimefrontfjella, Dronning Maud Land. *Br. Antarctic Survey Bull.*, **11**, 49–57.